



S-scheme N-doped carbon dots anchored $\text{g-C}_3\text{N}_4/\text{Fe}_2\text{O}_3$ shell/core composite for photoelectrocatalytic trimethoprim degradation and water splitting

Van Dien Dang ^{a,b}, Thamilselvan Annadurai ^c, Akhil Pradiprao Khedulkar ^c, Jui-Yen Lin ^c, Joemer Adorna Jr ^c, Wan-Ju Yu ^c, Bidhan Pandit ^d, Trung Viet Huynh ^e, Ruey-An Doong ^{e,*}

^a Institute of Environmental Engineering, National Yang Ming Chiao Tung University, 1001 University Road, Hsinchu 30010, Taiwan

^b Faculty of Biology - Environment, Ho Chi Minh City University of Food Industry, 140 Le Trong Tan St, Tan Phu dist, Ho Chi Minh 700000, Viet Nam

^c Department of Biomedical Engineering and Environmental Sciences, National Tsing Hua University, Hsinchu 30013, Taiwan

^d Department of Materials Science and Engineering and Chemical Engineering, Universidad Carlos III de Madrid, Avenida de la Universidad 30, 28911 Leganés, Madrid, Spain

^e Institute of Analytical and Environmental Sciences, National Tsing Hua University, Hsinchu 30013, Taiwan

ARTICLE INFO

Keywords:
Photoelectrocatalysis degradation
Trimethoprim
Hydrogen production
Carbon dots
S-scheme

ABSTRACT

Photoelectrocatalysis is a promising technique for energy conversion and environmental treatment. This study describes the photoelectrocatalytic (PEC) degradation of trimethoprim and hydrogen evolution using a photoanode prepared by N-doped carbon dots (NCD) incorporated $\text{g-C}_3\text{N}_4/\alpha\text{-Fe}_2\text{O}_3$ (CNFO) shell/core nanocomposite. The electrochemical analysis reveals that the photocurrent density of NCD@CNFO photoanode reached 3.07 mA cm^{-2} at 1.6 V vs. NHE , which is 4 and 15 times greater than that of CNFO and intact $\alpha\text{-Fe}_2\text{O}_3$, respectively. In the presence of peroxymonosulfate (PMS), the NCD@CNFO photoanode enabled 95 % and 90 % of trimethoprim (TMP) degradation in aqueous solution and lake water, respectively. Hydrogen generation coupled with TMP degradation was also observed in the PEC system, where the H_2 generation rate was $550 \mu\text{mol cm}^{-2} \text{ h}^{-1}$. Both superoxide (O_2^\cdot) and hydroxyl (OH^\cdot) radicals played a significant role in the degradation of TMP. The achievements could be assigned to the excellent photoabsorption and electron transfer properties of NCD, which enhanced the PEC activity of CNFO by enabling the S-scheme heterojunction to reduce electron-hole recombination. Moreover, PMS served as a cathodic electron acceptor to improve the catalytic properties of NCD@CNFO photoanode, demonstrating its contribution to both water treatment and hydrogen production. Such superior efficiency offers great potential to develop a PEC system using carbon dots/semiconductor hybrid catalysts for antibiotic degradation and synchronous photocatalytic H_2 evolution from wastewater, providing an alternative solution to environmental pollution and energy crisis issues.

1. Introduction

The energy scarcity and environmental pollution that originate from the increase in population and industrial activities have triggered the research need for renewable energy production and environmental treatment technologies. The emerging pollutants, especially residual and unmetabolized antibiotics, which have been discharged into water and soil, severely affect both the ecosystem and human health [1]. Trimethoprim (TMP) is an antibiotic commonly used for the treatment of bacteria-related diseases. It is estimated that around 80 % of TMP cannot be metabolized by the human body, causing a large amount of

TMP to enter the environment after excretion [1]. As biological or physicochemical processes in wastewater treatment plants cannot eliminate antibiotics completely, it is of great interest to develop an effective technique to remove antibiotics from wastewater systems. Moreover, for environmental protection, exploring clean and sustainable energy sources to replace fossil fuels is essential to achieve a low carbon society. Hydrogen produced from water splitting has been recently considered an eco-friendly energy carrier to replace fossil fuels in the near future. However, hydrogen production from water electrolysis is not an economical strategy due to its energy-intensive consumption and low gas evolution rate [2]. Therefore, developing a

* Corresponding author.

E-mail address: radoong@mx.nthu.edu.tw (R.-A. Doong).



cost-effective and efficient system for simultaneous contaminant removal and hydrogen production is a growing demand.

The solar light-driven photoelectrochemical technique (PEC) has been extensively applied to convert solar energy into renewable hydrogen energy and to abate contaminants because of its advantages in both photo- and electro-catalysis [3,4]. To this extent, pollutants are oxidized by the photogenerated holes at the photoanode, while hydrogen is produced by photoelectrons at the cathode. The efficiency of a PEC system is predominantly identified by its charge separation and transfer capacity. Hence, fabricating suitable materials for a PEC system is highly desirable for large-scale applications. Together with the bandgap requirements for high conversion performance, the photoelectrode materials applied in PEC must be widely available, highly light-harvesting, long-term withstand, and environmentally sustainable [5].

Among the emerging semiconductors, graphitic carbon nitride ($\text{g-C}_3\text{N}_4$) sparked its great potential in the application of photocatalysis and PEC due to its advanced properties such as non-toxicity, high stability, low cost, large surface area, and a suitable visible-light harvesting bandgap (2.7 eV) [6,7]. Nevertheless, $\text{g-C}_3\text{N}_4$ has shown its weakness with the high recombination rate of electron-hole pairs and low conductivity, leading to low photocatalytic efficiency. Therefore, a solution of integrating $\text{g-C}_3\text{N}_4$ with other suitable semiconductors to form a heterojunction that can suppress the recombination and enhance the photocatalytic efficiency has been proposed. In addition, $\text{g-C}_3\text{N}_4$, which has a relatively negative conduction band (CB) potential of 1.57 eV, can combine with another deep-valence band (VB) semiconductor to constitute a good charge carrier with strong redox ability. Hematite ($\alpha\text{-Fe}_2\text{O}_3$, FO) is a promising candidate for combining with $\text{g-C}_3\text{N}_4$ to form a composite photocatalyst due to its deep valence band (2.48 eV), highly photochemical stability, abundance, and environmentally benignity. However, corrosion or dissolution of the metal oxide $\alpha\text{-Fe}_2\text{O}_3$ during the PEC operation could diminish its activity. Fortunately, $\text{g-C}_3\text{N}_4$ was proved to have high chemical stability and outstanding mechanical, electrical, thermal, and optical properties [8]. Besides, the shell thickness could be tailored to tune light absorption. The increase of shell thickness was even proved to extend the light absorption to the longer wavelengths for composite catalysts, resulting in a better catalytic performance [9]. It was also reported that the core-shell nanostructured photocatalysts could lower the band gap energy, slow down electron-hole pair recombination rate, and accelerate electron transfer [10]. Thus, we aimed to prepare a highly efficient core/shell-type composite, in which C_3N_4 was a shell to protect Fe_2O_3 core from corrosion or dissolution as well as to provide synergistic result and stabilize the active nanoparticles. The nitrogen pairs in the heptazine ring of $\text{g-C}_3\text{N}_4$ render self-assembly with $\alpha\text{-Fe}_2\text{O}_3$ through the electrostatic complexation, which is the premise of assembling $\text{g-C}_3\text{N}_4$ and $\alpha\text{-Fe}_2\text{O}_3$ for a robust composite [11]. Various solid-state Z-scheme $\text{g-C}_3\text{N}_4/\alpha\text{-Fe}_2\text{O}_3$ composites have been engineered for pollutant photodegradation and hydrogen evolution [12–18]. Although Z-scheme photocatalysts exhibit their efficiency in suppressing electron-hole recombination, it is hard to achieve constant equilibrium in the electron-donating and accepting ability of the mediator [19]. Also, the loss of charge carriers in Z-scheme decrease the durability of photocatalytic activity [20]. To overcome these issues, it is needed to develop novel visible-light active components that can integrate with $\text{g-C}_3\text{N}_4/\alpha\text{-Fe}_2\text{O}_3$ to form highly efficient step-scheme (S-scheme) hybrid photocatalysts for efficient charge separation along with strong redox capability.

Carbon dots (CD), which possess a tunable bandgap and unique charge transfer and storage ability, are promising components for various applications, especially hydrogen generation and contaminant photodegradation [21,22]. Moreover, it was documented that nitrogen doping could increase the light absorption and electrical transfer of CD, which are beneficial to PEC activity [23,24]. Several studies evidenced that doping CD with nitrogen can considerably alter its band structure

and optoelectronic transport properties, enhancing catalytic activity toward photo-driven reactions [25,26]. Accordingly, owing to excellent electron transport capability, nitrogen-doped carbon dots (NCD) could play as a mediator to boost charge carrier separation, which is beneficial for improving PEC performance. Several studies have reported that incorporating NCD with other semiconductors can ameliorate their PEC hydrogen generation and pollutant removal performance [27–29]. Thus, we expect that NCD will be of benefit to improving the PEC activity of the $\text{g-C}_3\text{N}_4/\alpha\text{-Fe}_2\text{O}_3$ composite, which, however, has not been reported yet.

Towards this concept, we constructed an S-scheme NCD@ $\text{g-C}_3\text{N}_4/\text{Fe}_2\text{O}_3$ shell/core nanocomposite (NCD@CNFO) for both TMP degradation and hydrogen production. In this way, we propose that the internal electric field at the interfaces of components can speed up the charge transfer with the assistance of NCD, leading to the efficient utilization of electrons at the conduction band of $\text{g-C}_3\text{N}_4$ and holes at $\alpha\text{-Fe}_2\text{O}_3$. The morphology of NCD@CNFO in [Scheme 1](#) shows that 3-D hexagonal $\alpha\text{-Fe}_2\text{O}_3$ nanoplates with diameters of 150–200 nm were coated by $\text{g-C}_3\text{N}_4$ nanoflakes, while NCD anchored onto the surface of CNFO. Exploring the characterization and the performance of NCD@CNFO toward photodegradation of TMP and hydrogen evolution is the key focus of this study. NCD@CNFO nanocomposite demonstrated its photostability after 5 cycles of photocatalytic experiments. The task of each component and underlying mechanism were specified for the pollutant degradation and hydrogen production activities.

2. Experimental

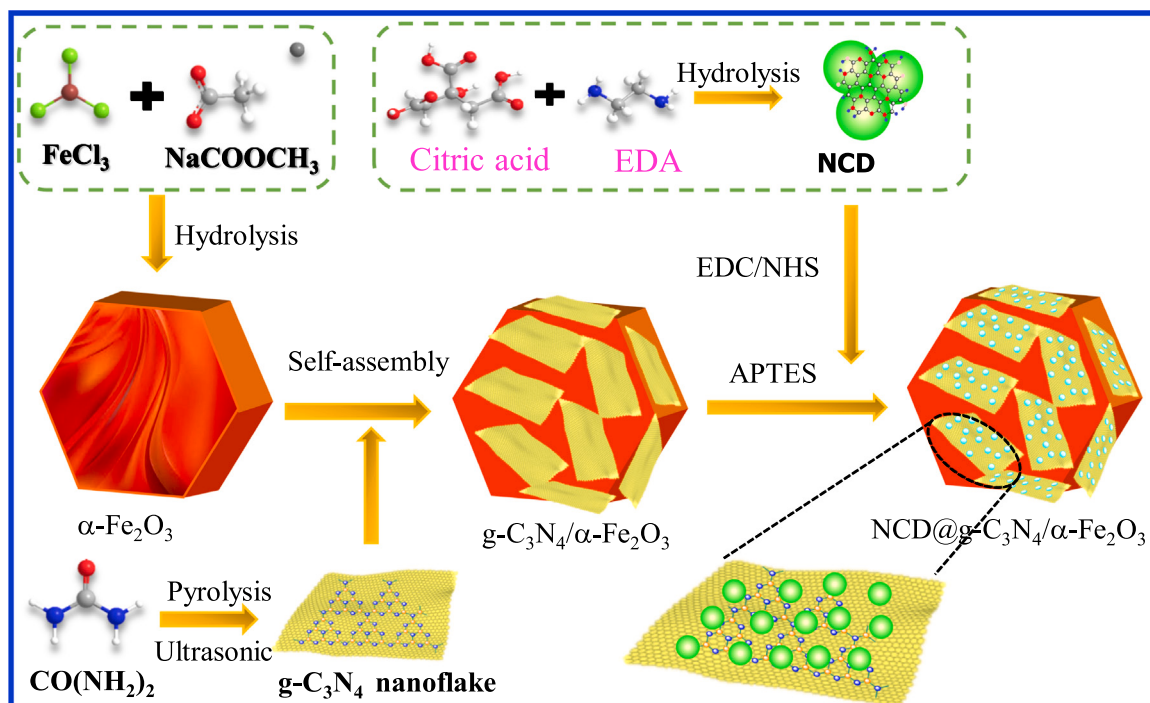
2.1. Fabrication of NCD@CNFO

The detailed experimental procedures as well as surface characterization approaches for NCD@CNFO can be found in [Supplementary data](#). Briefly, the hexagonal $\alpha\text{-Fe}_2\text{O}_3$ nanoplate (FO) was hydrothermally synthesized at 180 °C for 12 h in the presence of 1.0 mmol of $\text{FeCl}_3\cdot 6\text{H}_2\text{O}$ and 1.0 mmol of sodium acetate in 10 mL of ethanol. The $\text{g-C}_3\text{N}_4$ nanoflake (CN) was prepared by ultrasonication of bulk $\text{g-C}_3\text{N}_4$ in ethanol for 3 h. The $\text{g-C}_3\text{N}_4/\text{Fe}_2\text{O}_3$ (CNFO) shell/core nanocomposite was prepared through self-assembly by dropwise addition of 50 mg $\text{g-C}_3\text{N}_4$ nanoflake into 100 mg Fe_2O_3 , subsequently dried and calcined at 500 °C for 5 h. The NCD was fabricated using citric acid and ethylenediamine as the precursors at 120 °C in an oil bath. NCD@CNFO nanocomposite was prepared by conjugation of carboxylic groups on NCD with amine groups of (3-aminopropyl)-triethoxysilane (APTES) coated CNFO via EDC/NHS reaction.

2.2. TMP degradation and H_2 evolution

The PEC experiments were conducted in a quartz cell with 80 mL of 0.1 M Na_2SO_4 as the electrolyte. A three-electrode configuration that used Pt wire and Ag/AgCl electrode as the counter and reference electrodes, respectively, was coupled with a 100 mW cm^{-2} Xenon lamp equipped with a UV cut-off filter. The fluorine-doped tin oxide (FTO) conductive glass ($2 \times 1 \text{ cm}^2$) was used as the substrate of the working electrode, which was prepared by dispersing 3 mg of NCD@CNFO and black carbon in 1 mL of DMF onto FTO glass ($1 \times 1 \text{ cm}^2$). The detailed procedure for preparing the working electrode can be found in [Supplementary data](#).

The degradation of TMP over the NCD@CNFO based electrodes was studied using the PC, EC, and PEC systems. 1 mM of peroxymonosulfate (PMS) was added to the PEC cell to evaluate the effect of PMS on TMP removal efficiency. The aqueous concentration and intermediates of TMP were analyzed by high-performance liquid chromatography (HPLC) at 254 nm and HPLC-MS, respectively. Moreover, the hydrogen evolution from water splitting was carried out in a PEC quartz cell. The evolved H_2 gas in the cell was collected using a micro pump connected through closed pipes to gas chromatography. The detailed PEC



Scheme 1. Illustration of the synthesis procedure of NCD@CNFO nanocomposite.

procedures for TMP photodegradation and H₂ evolution over NCD@CNFO can also be found in [Supplementary data](#).

3. Results and discussion

3.1. Characterization of NCD@CNFO based photocatalysts

The morphologies of NCD were studied using transmission electron microscopy (TEM) and high resolution TEM (HRTEM). **Fig. 1a**, shows that the as-prepared NCD was homogeneously distributed, whereas their

corresponding particle size distribution histogram (inset of **Fig. 1a**) illustrates that the particle size of NCD was in the range of 3–9 nm with an average diameter of 7 nm. The HRTEM image of NCD in **Fig. 1b** shows the lattice spacing of 0.24 nm, corresponding to the (100) plane of single crystalline graphitic carbon dots [30]. The Fast Fourier transform (FFT) pattern in the inset of **Fig. 1b** further demonstrates the sp² graphite diffraction. The crystalline nature of the as-prepared NCD was evaluated by X-ray diffraction (XRD). In **Fig. 1c**, the XRD pattern of NCD shows a diffraction peak at 23°, corresponding to the crystal lattice distance of (002), which is a typical feature of carbon-based materials. Raman

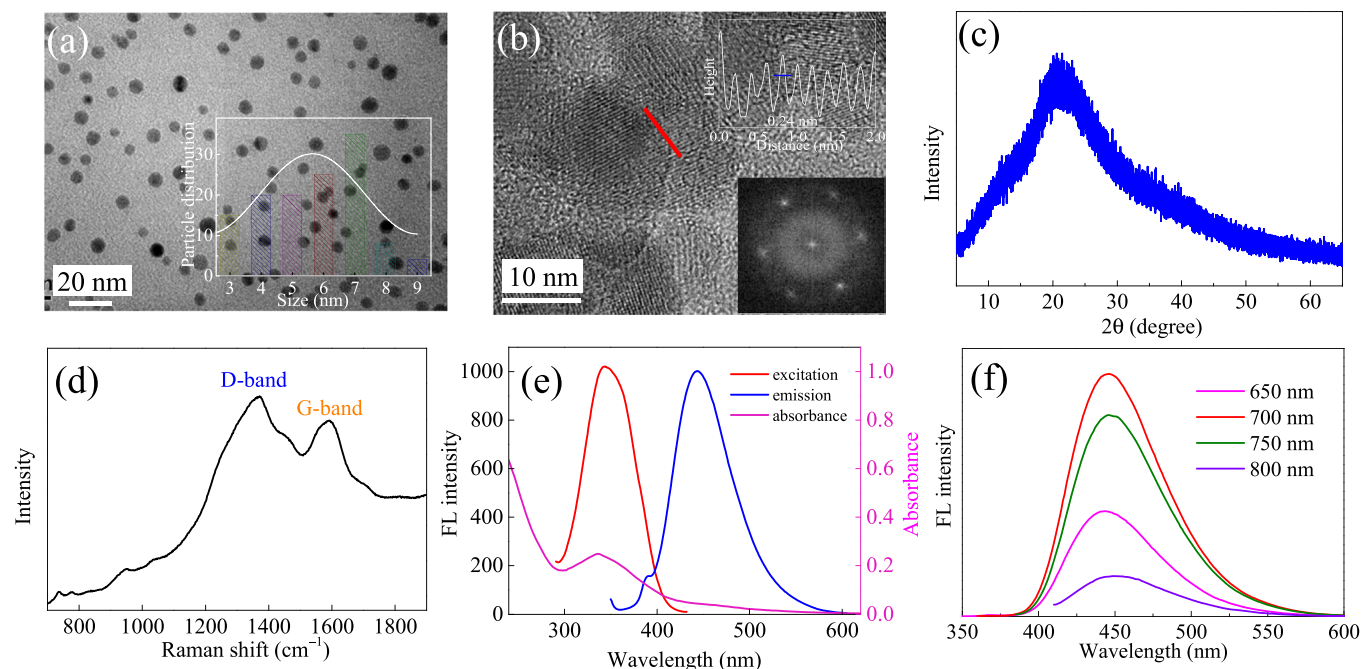


Fig. 1. (a) TEM (inset: particle size distribution), (b) HRTEM images (inset: lattice spacing and FFT pattern), (c) XRD pattern, (d) Raman spectra, (e) UV-vis and FL spectra, (f) up-converted FL spectra of NCD.

spectroscopy was utilized to learn the detailed information about chemical structure, crystallinity, and molecular interactions of NCD. As shown in Fig. 1d, the disordered structure (D-band) related to the presence of sp^3 defects, and crystalline structure (G-band) associated with the in-plane vibration of sp^2 carbon of NCD can be observed in the Raman spectra at 1372 and 1589 cm^{-1} , respectively [31]. The ratio of the intensity (I_D/I_G) of 0.86 suggests that the as-prepared NCD was a crystalline and graphitic material [32].

Fluorescence (FL) measurement was used to explore photoinduced charge carrier excitation and transfer over NCD. In Fig. 1e, the UV-visible spectrum of the as-prepared NCD featured an absorption at 345 nm which can be appointed to the $n-\pi^*$ transitions of $C=O/C=N$ functional groups. FL excitation/emission spectra display that an emission peak at 445 nm was obtained under irradiation at 345 nm. Furthermore, the upconverted FL spectra were examined by FL spectroscopy using different excitation wavelengths (650–850 nm). In Fig. 1f, NCD shows its excellent upconversion property since it could absorb visible light at longer wavelengths, then emitted FL at shorter wavelengths. In other words, the NCD is vital in collecting and transferring energy to CNFO nanocomposite to promote the generation of electron-hole pairs, and to enhance the PEC performance.

The morphologies of NCD@CNFO based composites were examined using scanning electron microscopy (SEM), TEM, and HRTEM. For FO, the hexagonally crystalline nanoplates with a length of 160 ± 14 nm and a thickness of 40 ± 8 nm were observed (Fig. 2a and b). The plate-like morphology of FO has several advantages: (1) the large ab -plane can form vast heterojunctions with $g\text{-C}_3\text{N}_4$ flakes, which can be regarded as a 2-D material; and (2) the relatively small thickness of FO can minimize the recombination of electrons and holes as the hole diffusion length of hematite is only 2–4 nm [33]. The HRTEM image of FO in Fig. 2c

signifies that the microstructure was highly crystalline with an interplanar d-spacing of 0.37 nm, which is consistent with the (120) lattice plane of hexagonal $\alpha\text{-Fe}_2\text{O}_3$ [17]. The single crystallinity of FO is shown by the selected area electron diffraction (SAED) pattern in the inset of Fig. 2c. The existence of six equivalent corresponds to the [001] direction which is perpendicular to the facets of hexagonal nanoplates, indicating the exposed facets is (001) [17].

The morphology of pure CN was also investigated using SEM and TEM images. Fig. 2d–e illustrate that two dimensional nanoflakes with the size about 50–100 nm. Fig. 2f reveals the layered structure of CN with inter-planar d-spacing of 0.32 nm. The SEM image of CNFO in Fig. 2g shows that FO particles were fully covered by $g\text{-C}_3\text{N}_4$ on the surface to form a shell/core structure, in which FO was the core and CN was the shell. The strong attachment between FO and CN can be ascribed to electrostatic forces during self-assembly. Notably, the shell/core structure of CNFO indicates the intimate interaction between the core FO and the shell $g\text{-C}_3\text{N}_4$ nanoflake, leading to the same shape as FO, but the size was increased by 40 nm in diameter. Several studies have reported the shell/core nanostructure of hematite and $g\text{-C}_3\text{N}_4$, and such tight conjunctions could easily enable the direct/indirect Z-scheme heterojunctions [15,34].

The TEM image of NCD@CNFO (Fig. 2h) reveals the well-dispersion of NCD on the CN shell that covers the FO core. Likewise, the HRTEM image of NCD@CNFO shown in Fig. 2i confirms a lattice distance of 0.24 nm, which is indexed to the (100) plane of NCD [35]. Moreover, two distinct lattice fringes with d-spacings of 0.32 and 0.25 nm were observed, which comply with the (002) lattice plane of CN and (012) plane of FO, respectively [11,17]. The FFT (the inset of Fig. 2i) shows a particular annular region, depicting a hexagonal pattern similar to the SAED results. This result clearly indicates that both $\alpha\text{-Fe}_2\text{O}_3$ and NCD are

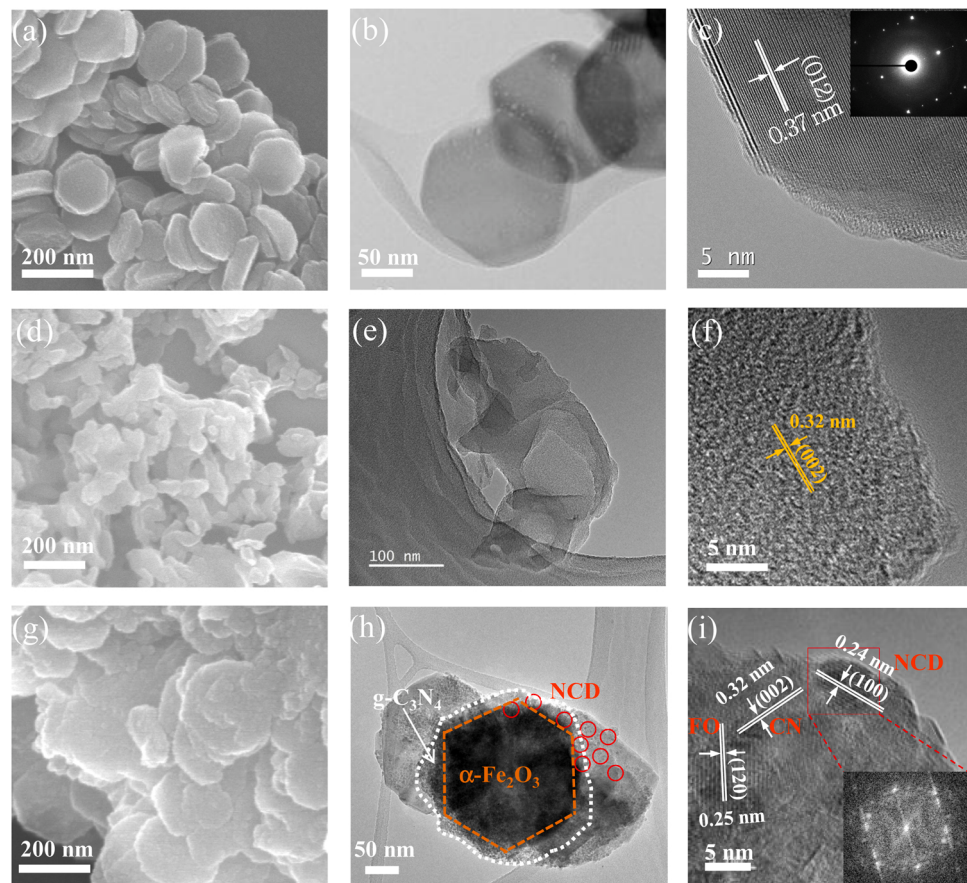


Fig. 2. (a) SEM, (b) TEM, and (c) HRTEM images of FO; (d) SEM, (e) TEM, and (f) HRTEM images of CN; (g) SEM, (h) TEM, and (i) HRTEM images of NCD@CNFO. Inset of (c) is SAED pattern, and inset of (f) is FFT pattern.

attached closely onto hexagonally sp^2 graphitic carbon. To further investigate the elemental distribution of the NCD@CNFO catalyst, the scanning TEM images and elemental maps were studied. Energy-dispersive X-ray spectroscopy (EDX) mapping results (Fig. S1, Supplementary data) show the homogeneous distribution of C, N, O, and Fe elements on NCD@CNFO with weight percentages of 48.1, 12.4, 27.3, and 12.2 wt%, respectively. In sum, the interaction between NCD, FO, and CN resulted in the successful formation of NCD@CNFO composite with a rough surface, providing more active sites for PEC reactions.

X-ray diffraction (XRD) was performed to shed more light on the crystallography of the as-prepared NCD@CNFO based composites. As presented in Fig. 3a, the XRD patterns of FO-containing samples show sharp diffraction at 20 of 24.4°, 33.4°, 35.9°, 41.1°, 49.7°, and 54.2°, corresponding to the standard pattern of α -Fe₂O₃ at (012), (104), (110), (113), (024), and (116) planes, respectively (JCPDS 33-0664) [14,15]. The existence of a peak at 27.6° 20 is related to the (002) conjugated aromatic ring of interlayer stacking of CN [36]. On the contrary, the diffraction of g-C₃N₄ was absent in the XRD patterns of CNFO and NCD@CNFO because of the poor crystallinity of CN and its relatively low proportion. The diffraction peak at 20 of 23.7° of NCD@CNFO is likely from the NCD bound to CNFO by EDC/NHS reaction. Notably, the hematite peaks of NCD@CNFO shifted downward by 0.4° compared to the peaks of FO and CNFO. It can be ascribed to the incorporation of NCD in the CNFO shell/core structure, causing a change in stoichiometric proportions as well as a shift in diffraction angle to a lower position.

The fluorescence lifetime of the as-prepared nanocomposites was analyzed to explore the dynamics of photo-excited charge carriers of FO, CNFO, and NCD@CNFO (Fig. 3b). The emission decay of pure FO had an average lifetime of 1.38 ns, which is much shorter than those of CNFO (2.33 ns) and NCD@CNFO (2.69 ns). This elaborates that the CNFO

prolonged the lifetime of the photo-excited carriers by the formation of direct Z-scheme heterojunction, where the fast charge recombination within FO and CN could be inhibited [17]. In the presence of NCD, the direct Z-scheme would shift to an S-scheme as the NCD serves as an electron mediator due to its superior conductivity. Therefore, electrons in FO would recombine with holes in CN via the mediation of NCD, which in turn isolates the holes and electrons in FO and CN, respectively, and further prolonged the lifetime of the photo-excited carriers.

The specific surface area and pore properties of the as-prepared NCD@CNFO nanocomposite were calculated using Brunauer-Emmett-Teller (BET) method. Fig. 3c displays the N₂ adsorption/desorption curves of CN, FO, CNFO, and NCD@CNFO. The CN possessed a large BET surface area ($38.7 \text{ m}^2 \text{ g}^{-1}$) owing to its laminar structure. The relatively low specific surface area ($8.5 \text{ m}^2 \text{ g}^{-1}$) and the type IV isotherm with H3 hysteresis loop of FO presented the mesoporous characteristic with silt-like pores of metal oxides [37]. The presence of FO reduced the specific surface area of CN to $24.6 \text{ m}^2 \text{ g}^{-1}$, which was probably due to the attachment between the CN shell and the FO core during the formation of the CNFO shell/core structure. A slight increase in S_{BET} of NCD@CNFO ($30.2 \text{ m}^2 \text{ g}^{-1}$), compared to that of CNFO, might be attributed to etching and oxidation during hydrothermal synthesis [35]. The Fe K-edge X-ray absorption near-edge structure (XANES) spectra of nanomaterials is shown in Fig. 3d. The absorption edge of FO located at 7135 eV was obviously overlapped with CNFO, suggesting that the Fe atoms carry positive charges has no change after forming a cluster with C₃N₄. However, the spectra intensity increases after doping with NCD, likely attributed to the replacement of Fe-O-Fe by the functional groups of NCD to form Fe-O-N or Fe-O-OH. This result is a strong indicator for pre-edge peak of Fe, which comes from the electronic 1 s→3d transition in Fe³⁺ on tetrahedral lattice sites.

Fourier transform infrared spectroscopy (FTIR) analysis was performed to gain awareness of the functional groups on NCD. The FTIR

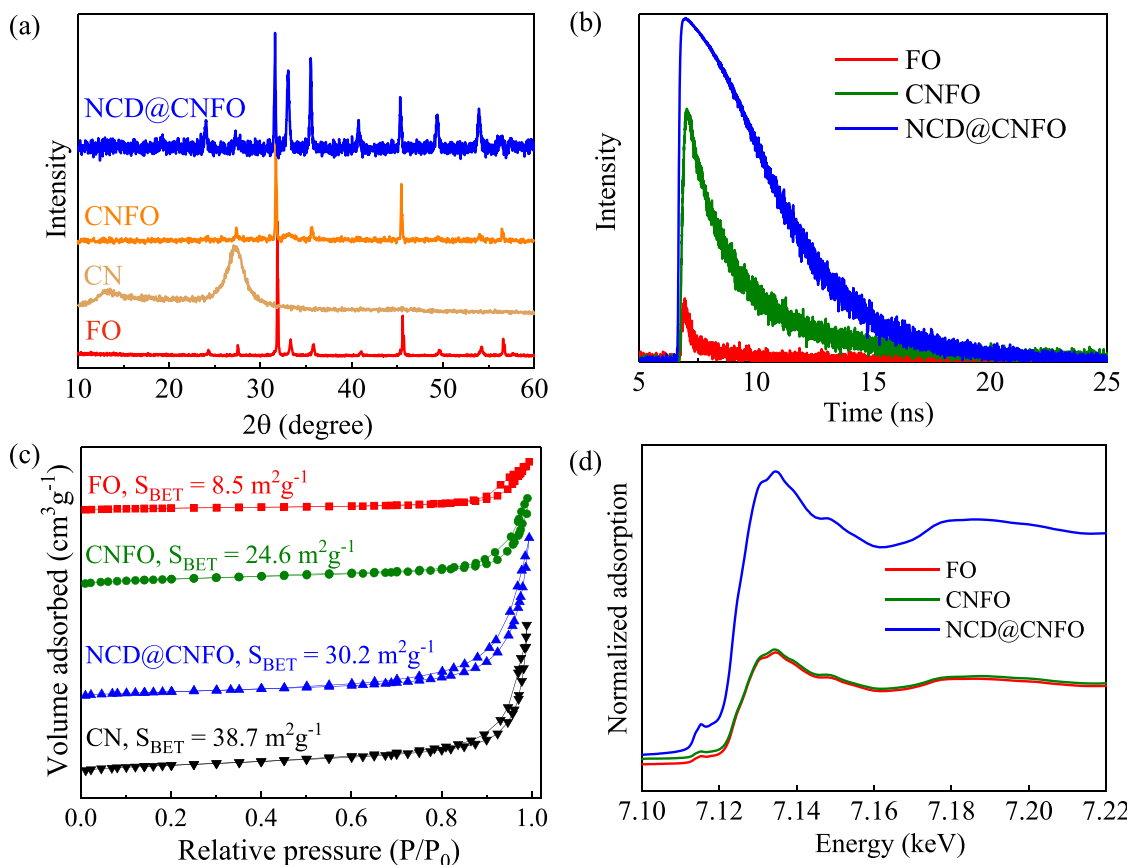


Fig. 3. (a) XRD patterns, (b) Fluorescence life-time, (c) N₂ adsorption-desorption curves, (d) Fe K-edge XANES for FO, CNFO and NCD@CNFO.

spectra (Fig. S2, *Supplementary data*) show that FO exhibited several characteristic vibrations, including the stretching of the surface hydroxyl group (3450 cm^{-1}), vibrations of the carboxylate group from the adsorbed acetate (1630 and 1420 cm^{-1}), and the inherent lattice vibration of hematite (400 – 800 cm^{-1}) [38]. After combining FO with CN, the vibrations of $\text{g-C}_3\text{N}_4$ including the triazine unit at 805 cm^{-1} and the uncondensed N–H groups between 2850 and 3450 cm^{-1} were revealed [18]. Lastly, the introduction of NCD brought about the bands between 1200 and 1700 cm^{-1} that are the vibrations of C–H (1375 and 1450 cm^{-1}), C–N (1540 cm^{-1}), CO=NH (1650 cm^{-1}), and N–H (3280 cm^{-1}) [39]. Therefore, the FTIR spectra confirm the presence of adsorbed species for NCD@CNFO.

The XPS measurement was carried out to evaluate the compositional framework and surface states of the nanocomposites. The survey spectra in Fig. S3a (*Supplementary data*) show the peaks of C 1s (287.7 eV), N 1s (398.2 eV), and O 1s (529.3 eV) for CNFO and NCD@CNFO. Moreover, two distinct peaks in the region of 705 – 730 eV were ascribed to the core-level peaks of iron (Fe 2p) from FO. Aside from the expected O 1s and Fe 2p peaks, the existence of an interstitial C 1s peak was also detected in the EDS spectrum of pure FO. This carbon impurity peak implies the existence of intercalated acetate (CH_3COO^-) ions in the $\alpha\text{-Fe}_2\text{O}_3$ crystal lattice during preparation, which has been reported for both naturally-made and synthetic hematite ions [40]. Likewise, no other elements were detected in the spectra of CNFO and NCD@CNFO. Fe 2p_{3/2} and Fe 2p_{1/2} envelopes were adjusted by two components (Fe^{2+} and Fe^{3+}), which were found to shift to lower energy after doping with CN and NCD. For example, the binding energies of Fe 2p_{3/2} are 709.9 eV for Fe^{2+} and 711 eV for Fe^{3+} , as shown in Fig. S3b (*Supplementary data*)

[11]. However, these energy peaks shifted to 709 and 711.4 eV for CNFO and 709.3 and 711.8 eV for the NCD@CNFO sample (Fig. 4a). Additionally, the shake-up satellite peaks found in 717.9 and 733.8 eV further validate the presence of Fe_2O_3 [17].

The high-resolution spectra for O 1s of NCD@CNFO shown in Fig. 4b comprise three peaks, i.e. Fe–O/C=O (528.1 – 529.2 eV), O–H overlapped with C–O (529.8 – 531.2 eV) [17]. Moreover, the peaks at 533.1 eV and 535.3 eV represent for O=C–O bond and C–O of NCD [35]. As displayed in Fig. S3c (*Supplementary data*), the O 1s peaks existed almost indistinctively for FO and CNFO. However, the peaks for FO shifted slightly to lower binding energy for CNFO. For example, Fe–O peak at 529.2 eV for FO shifted to a lower energy at 528.1 eV for CNFO, illustrating the binding effect of the carbon structure of the CN shell on the FO core. It is noteworthy that the Fe–O peak at 528.1 eV for CNFO in turn moved backwards to higher binding energy at 528.9 eV for NCD@CNFO, confirming the existence of strong interaction between NCD, CN, and FO [41]. Fig. 4c shows the C 1s core-level spectra of NCD@CNFO, in which two prominent peaks coming from C=C/C–C (284.3 eV) and N–C=O (287.3 eV) were ascribed to sp^3 -bonded carbon of graphite and $\text{g-C}_3\text{N}_4$ [35,42]. The intensity of N–C=O for NCD@CNFO was relatively higher than CNFO and pure FO (Fig. S3d, *Supplementary data*), which is likely due to the presence of NCD. Likewise, the N–C peak in the N 1s peaks centering at 397.4 eV was found for both CNFO and NCD@CNFO, as shown in Fig. 4d and Fig. S3e (*Supplementary data*). Moreover, the peak at 399.7 eV corresponds to the binding energy of sp^2 hybridized N in C=N–C [14]. The peak at 404.3 eV was attributed to graphitic N of C_3N_4 [43]. The left-leaning shift of the NCD@CNFO peaks of N 1s could be caused by the

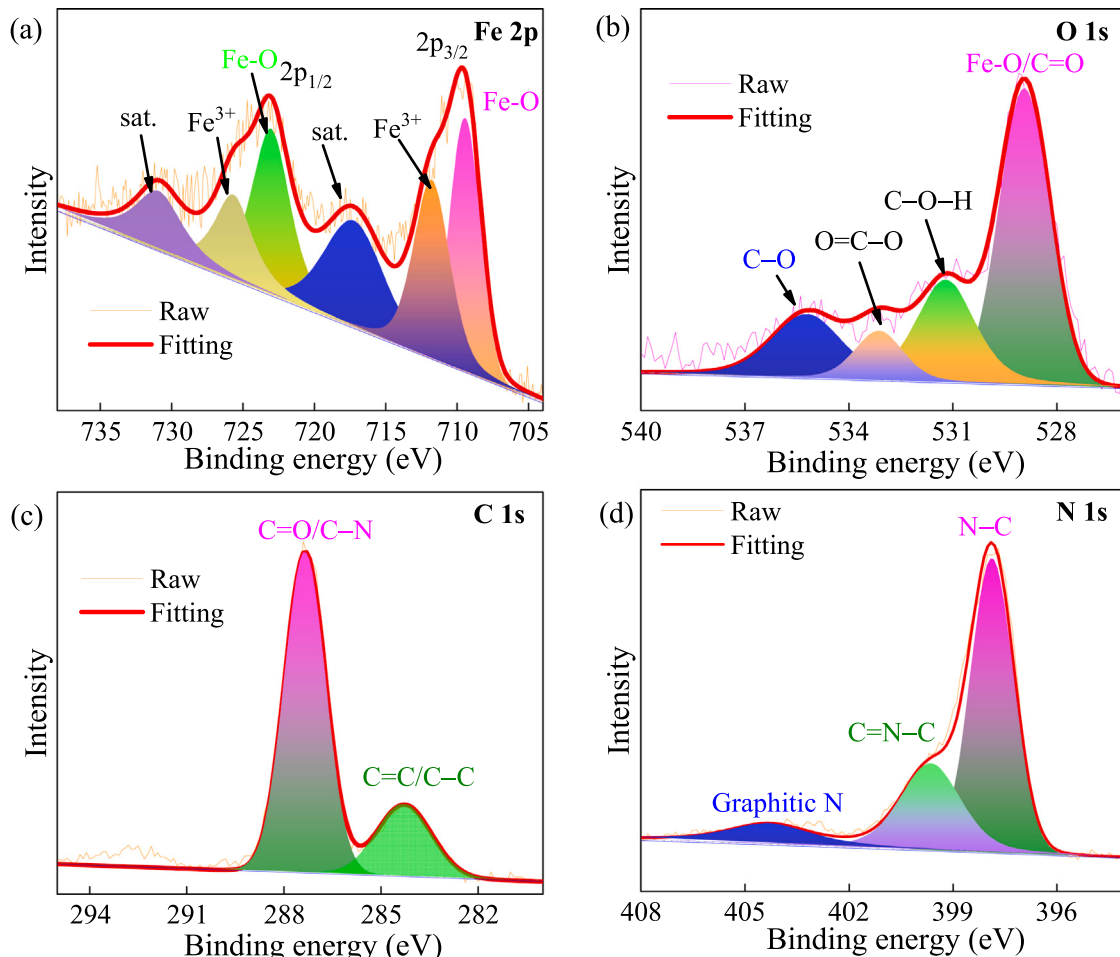


Fig. 4. High-resolution XPS spectra of (a) Fe 2p and (b) O 1s, (c) C 1s, and (d) N 1s of NCD@CNFO.

incorporation of NCD.

3.2. Electrochemical and optical properties of NCD@CNFO

The electrochemical properties of NCD@CNFO based materials were further explored to understand their suitability as a PEC catalyst. The transient photocurrent curves of the as-prepared materials are displayed in Fig. 5a. The as-prepared photocatalysts exhibit reproducible photocurrent measurements after 6 illumination cycles. The photocurrent intensity of CNFO and FO were relatively low, being 0.8 and 0.2 mA cm^{-2} , respectively, at the 6th cycle. With the incorporation of NCD, the photocurrent density of NCD@CNFO increased to 3.07 mA cm^{-2} after 6 cycles, which was 4- and 15-folds higher than CNFO and FO, respectively. The photocurrent density achieved in this study was higher than CNFO composite from other studies, which were 0.09 [11], 5 [12], 0.15 [13], 10 [14], 6.0 [16], 0.18 mA cm^{-2} [44]. We attribute the improved photocurrent of the as-prepared photocatalyst to following reasons: (1) the tight interface between core FO and CN nanoflake shells allowed fast electron transfer from the conduction band of FO to the valence band of CN, suppressing the electron-hole recombination; (2) the excellent capability of NCD to serve as the light absorber and photogenerated charge carrier [11]; (3) NCD possesses an upconversion property, which was proved in the fluorescence spectra (Fig. 1f), allowing the NCD to absorb more photons from light sources for enhanced photocurrent density. Fig. S4a reveals the FL intensity of NCD@CNFO and its components in aqueous solution with the same concentration under the excitation wavelength of 750 nm. It is apparent that the NCD@CNFO showed the highest FL emission intensity at 450 nm compared to the remaining samples, confirming the upconversion property of NCD@CNFO. On the other hand, the doping of NCD provided more electrons in the conduction band along with FO, which could fully consummate the holes in the CN valence band, significantly improving the electron-holes separation efficiency as supported by the fluorescence lifetime spectra [16].

The electrochemical impedance spectroscopy (EIS) of the as-prepared nanocomposites was examined to evaluate the complex charge transfer resistance at the electrolyte-material interface. The charge transfer resistance (R_{ct}), which corresponds to the semi-arc in the high-frequency region (10^5 – 10^3 Hz), indicates the electron transfer resistance at electrode-electrolyte interface. As shown in Fig. 5b, the relative semi-arc magnitudes followed the sequence NCD@CNFO < CNFO < FO. The smallest impedance obtained in the NCD@CNFO nanomaterial proves that the heterostructure has the highest electron-hole separation ability and charge transfer efficiency. The equivalent circuit diagram was plotted using EIS spectrum analyzer to rationalize the charge transfer phenomena. The equivalent circuit (inset of Fig. 5b) includes solution resistance (R_s) and charge transfer resistance (R_{ct}) elements. The lowest value of R_{ct} for NCD@CNFO (85Ω) means that the electrical conductivity of this composite was the highest, compared to CNFO (260Ω) and FO (790Ω). Moreover, the small radius of NCD@CNFO signifies the low resistance during the migration of charges at interfaces as well as enhanced the contact conductivity between the as-prepared material and the electrolyte [45]. The EIS result corroborates that the doping of NCD into CNFO heterojunctions can improve the e^- - h^+ separation, inhibit charge carrier recombination, and increase the transfer efficiencies of photogenerated charge carriers [11,14].

The linear sweep voltammetry (LSV) spectrum of the as-prepared nanomaterials was determined to examine their surface reduction and photochemical hydrogen production ability. As shown in Fig. 5c, the high current density response of NCD@CNFO in comparison with CNFO and FO elaborates the higher separation efficiency of photogenerated e^- - h^+ pairs. This behavior is attributed to the abundant active sites on the NCD@CNFO surface. Furthermore, NCD anchored on the CNFO surface significantly improved the response current, and subsequently enhances the charge separation to increase the lifetime of electrons. The result shows that NCD@CNFO could be an excellent photocatalyst for highly efficient photoelectrochemical degradation of TMP as well as H_2 production. Moreover, the performance of PEC system was quantitatively

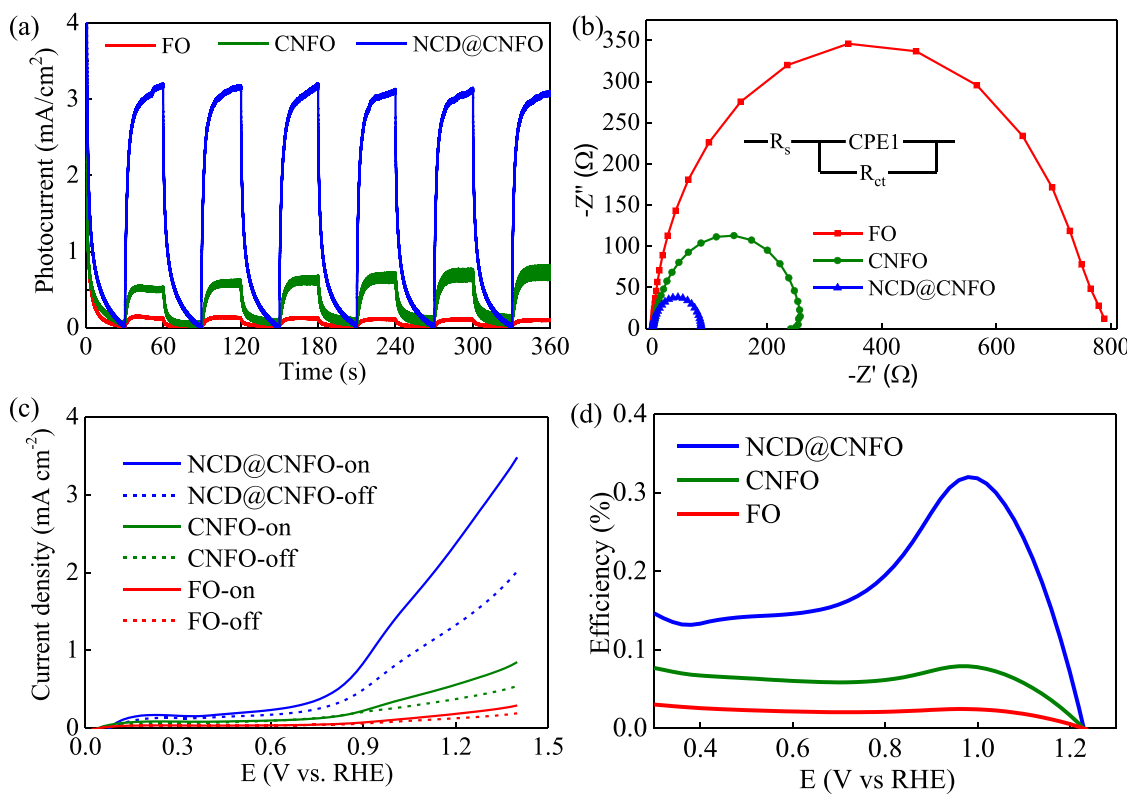


Fig. 5. (a) Photocurrent density, (b) Nyquist plot, (c) LSV polarization curve, and (d) photoconversion efficiency of FO, CNFO, and NCD@CNFO.

evaluated by photoconversion efficiency (PCE). As shown in Fig. 5d, the highest PCE of 0.32 % at 0.98 V vs. RHE was obtained in NCD@CNFO electrode. Under the same potential, the PCEs of CNFO and pure FO electrodes were only 0.08 % and 0.03 %, respectively. Thus, the enhanced PEC performance of the NCD@CNFO shell/core nanostructure clearly demonstrates a synergistic effect achieved by the NCD doping modification.

The optical properties of the nanocomposites were investigated through UV-vis absorption spectra measurement. As shown in Fig. S4b (Supplementary data), all the catalysts exhibit visible-region absorption ability. The addition of CN shell to the FO core caused a blue shift in the absorption edge, probably due to the exfoliation effects [46]. It is noted that the NCD@CNFO nanocomposite has a similar absorption edge with CNFO but higher absorption intensity. This result can be attributed to the fact that NCD can increase the optical path with multiple scattering effects [26]. Moreover, the intersection of the tangent and the plot were measured to be 597, 457, 599, and 594 nm for FO, CN, CNFO, and NCD@CNFO, respectively. Accordingly, the bandgaps of FO and CN were estimated as 2.06 and 2.80 eV, respectively.

3.3. PEC degradation of TMP over NCD@CNFO

The degradation of TMP over NCD@CNFO based nanocomposites was investigated under variable energy input conditions including PC, EC, and PEC with and without PMS to ascertain the crucial factors for the efficient degradation of TMP. Accordingly, the catalysts and their combination with PMS activation were tested through a series of experiments. The photolysis, electrolysis, and photoelectrolysis alone (without catalysts) showed negligible capability in TMP removal. Fig. 6a reveals that the degradation of TMP was quite low in PC condition over all catalysts, which are 10 %, 21 %, and 24 % for FO, CNFO, and NCD@CNFO, respectively. Fig. 6b shows that 33 % of TMP was removed

by NCD@CNFO in EC condition, which was higher than that achieved by FO (18 %) and CNFO (27 %) but the process was still insufficient. The combination of PC and EC to give PEC, as shown in Fig. 6c, has improved the removal efficiency of TMP, in which 25 %, 42 %, and 64 % of TMP was degraded over FO, CNFO, and NCD@CNFO, respectively. Furthermore, to investigate the self-degradation of PMS in the system, the control experiments of TMP removal with and without PMS in the photoelectrolysis (PE) were also conducted. As shown in Fig. 6d, a slight degradation efficiency of TMP was found in the presence of PMS (9 % in 60 min), which was higher than that in photoelectrolysis without PMS (5 % in 60 min, as displayed in Fig. 6c). This result signifies that the self-decomposition of PMS was poor without catalyst. With the further introduction of PMS into the system, the removal efficiency of TMP over FO, CNFO, and NCD@CNFO photocatalysts increased to 42 %, 75 %, and 97 % (Fig. 6d). This result was probably due to the electrochemical activation of PMS over those catalysts to improve the degradation of TMP [47].

The role of PMS in the degradation of TMP by other systems (PC and EC) was also confirmed over NCD@CNFO composite. The result shown in Fig. S5 signifies the significant improvement in degradation performance of all systems in the presence of PMS. The enhancement of photocatalytic performance with the addition of PMS to generate more reactive species has been reported elsewhere [48,49]. In all of the various energy input systems (PC, EC, and PEC), NCD has proved as an important ingredient in the composite to combine PEC-induced-charges from the conduction band of FO (electron) and the valence band of CN (hole), resulting in the inhibition of the recombination of electron-hole pairs in both CN and FO. Thus, more electrons and holes would be generated in the conduction band of CN and the valence band of FO to trigger the PEC degradation of TMP more readily. Compared to other FO- or CN-based PEC systems (Table S1, Supplementary data), the S-scheme NCD@CNFO gave the highest efficiency of antibiotic

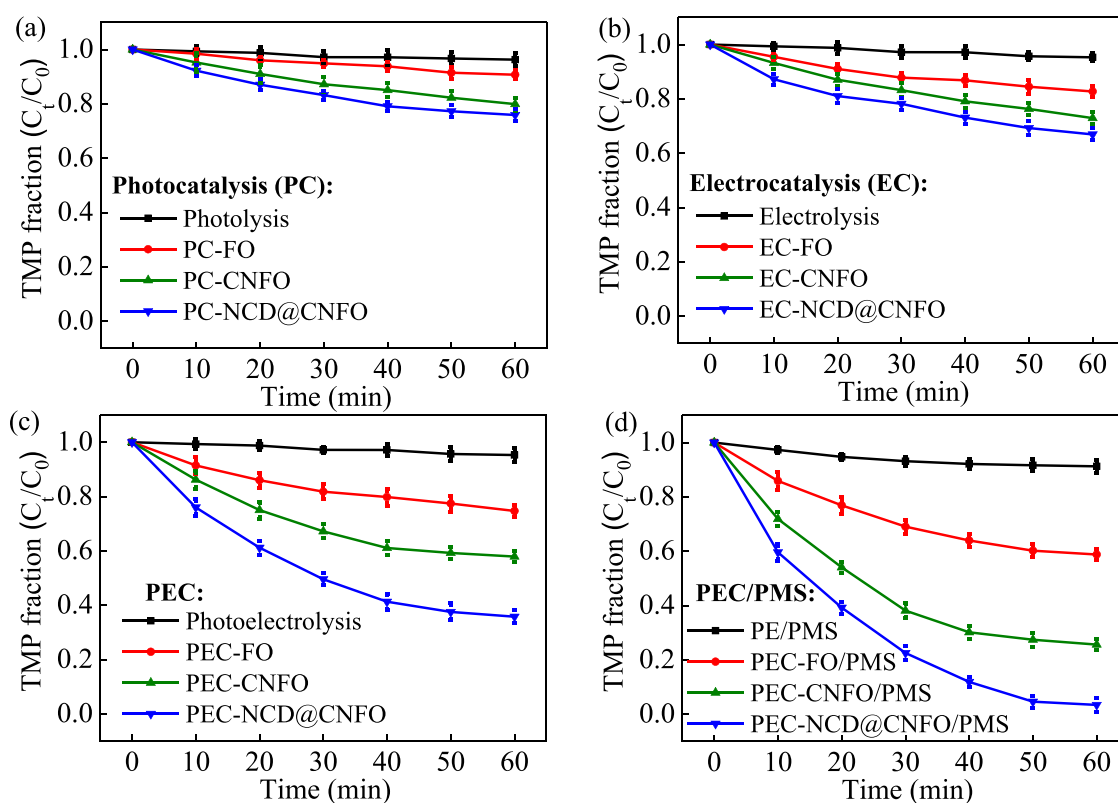


Fig. 6. (a) Degradation of TMP over various catalysts with (a) photocatalysis, (b) electrocatalysis, (c) photoelectrocatalysis, (d) photoelectrocatalysis/PMS. Conditions: [catalysts] = 285 mg cm⁻², [TMP] = 0.05 mM, [PMS] = 0.1 mM, [Na₂SO₄] = 0.1 M, illumination density: 100 mW cm⁻², pH = 5 ± 0.1, applied bias = 1.23 V vs. RHE.

degradation.

The effect of TMP concentrations on the degradation efficiency was tested by adding various concentrations (0.05–2 mM) of TMP to the PEC system. As shown in Fig. 7a, the degradation efficiency of TMP decreased as the initial concentration of TMP increased, which could be due to the insufficient production of reactive species and limited active sites on the catalyst surface. Moreover, the high TMP concentration could lead to low diffusion of mass transport of PMS toward the electrode surface, resulting in the poor production of radicals. The limited active surface of NCD@CNFO is also a factor to decrease the degradation efficiency at high concentrations of TMP. In addition, the intermediate products might compete with TMP at high concentrations [50]. The influence of PMS concentration on PEC degradation of TMP over NCD@CNFO is presented in Fig. 7b. The TMP degradation performance was improved when the concentration of PMS increased from 0 to 0.1 mM. Theoretically, more reactive radicals would be generated at higher PMS concentration. However, the efficiency decreased when the PMS concentration was higher than 0.1 mM. This phenomenon is attributed to the self-quenching of excessive PMS, which inhibited the generation of active radicals from the photocatalyst [51].

pH plays a crucial role in the PEC degradation of TMP over NCD@CNFO mediated PMS systems because it changes the surface charge of the photocatalyst and the protonation of TMP. In this work, the initial pH was adjusted from 3 to 11 by 0.1 M HCl or 0.1 M NaOH. Fig. 7c illustrates that the optimal pH for PEC degradation of TMP is 5. According to the zeta potential measurement, the as-prepared NCD@CNFO has an isoelectric point of 4.6, indicating that the surface charge of NCD@CNFO nanocomposite will be positive at pH < 4.6 and vice versa. In addition, TMP has two amino groups with pK_a values of 3.23 and 6.76 [52], meaning that it is a divalent cation at pH < 3.23, monovalent cation at pH between 3.23 and 6.76, and neutral species at pH > 6.76. Hence, the positive charge on the nanomaterial surface tended to repulse the positively charged TMP under acidic conditions at pHs 3–4, resulting in a low removal efficiency. In contrast, HSO_5^- is the dominant species of PMS at mild acidic condition at pH 5 [53], thus readily adsorbed on the

surface of NCD@CNFO. This condition triggered the electrostatic interaction between negative radicals (SO_4^{\bullet} and SO_4^{2-}) and protonated TMP, leading to the highly efficient degradation of TMP by HSO_5^- radicals. Under the basic conditions, however, the deprotonated TMP was hard to attach on the surface of NCD@CNFO, resulting in the low degradation performance. Moreover, Cl^- , NO_3^- , HCO_3^- , and $H_2PO_4^-$, which are ubiquitous in wastewater, usually have significant effects on degradation efficiency. They can inhibit the adsorption of contaminants on catalysts' surface or alter the degradation rate. Fig. 7d reveals the effects of 0.1 mM Cl^- , NO_3^- , HCO_3^- , and $H_2PO_4^-$, on TMP degradation over NCD@CNFO/PMS system. It is apparent that the PEC degradation of TMP decreased from 97 % to 95 % in the presence of 0.1 mM Cl^- , which has the lowest impact among other anions. The decrease in the degradation efficiency was due to the assumption of sulfate radicals SO_4^{\bullet} (generated from PMS) to oxidize Cl^- and form free chlorine species that have low oxidant capability. The effect of Cl^- anions was also proved to be negligible in a study of Zhang et al. [44].

The recycling capability of the NCD@CNFO PEC photocatalyst is an important standard for assessing its practical applicability. In this study, the PEC stability of NCD@CNFO was investigated through 5 consecutive cycles for simultaneous TMP degradation and H_2 production. As shown in Fig. 8a, the PEC efficiency of TMP degradation was 97 % for the 1st cycle, and then the degradation efficiency of TMP maintained in the range of 93.9–95.6 %. The excellent stability of NCD@CNFO was elaborated as the PEC activity toward TMP degradation. Furthermore, the lake water was used to examine the matrix effect of the solution on the photoelectrochemical performance of NCD@CNFO. The physicochemical properties of lake water were characterized and listed in Table S2 (Supplementary data). A suitable amount of TMP stock solution was spiked into the lake water to achieve the concentration of 50 μ M in the PEC quartz cell. The result illustrated in Fig. 8b (Supplementary data) signifies that the PEC activity of NCD@CNFO toward TMP degradation in lake water could achieve nearly the same as in an aqueous solution. The PEC activity could still maintain for at least 90 % of the initial activity, depicting that the NCD@CNFO catalyst has a high potential to be

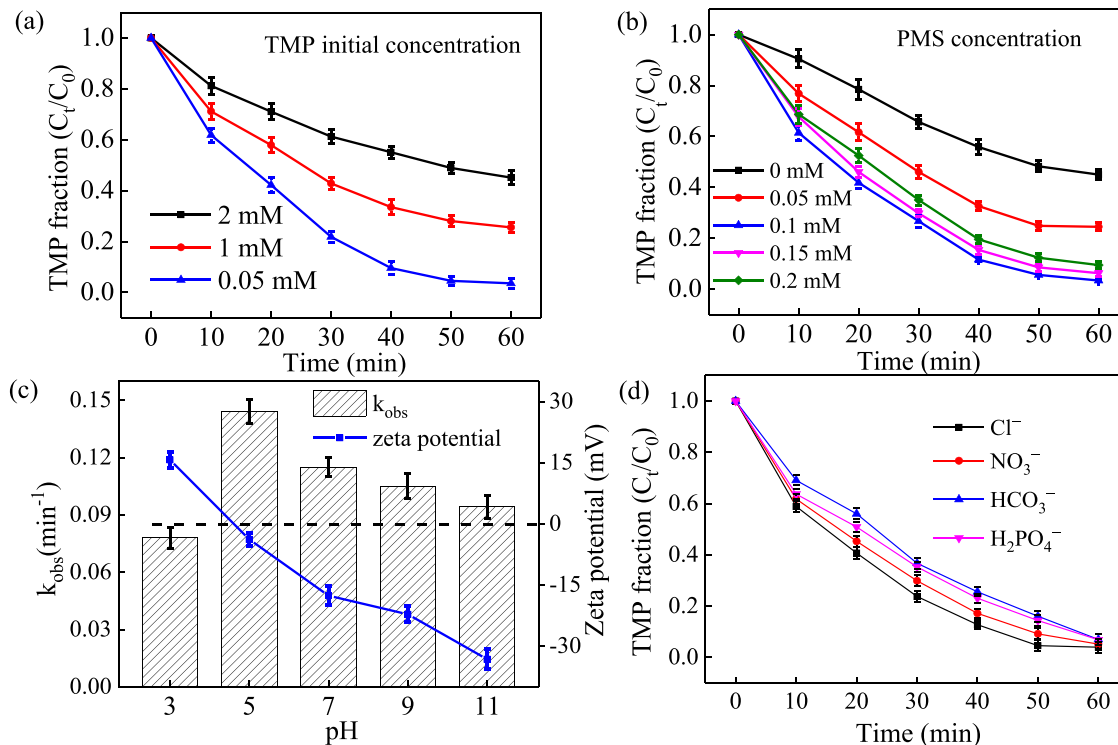


Fig. 7. (a) the effect of (b) TMP initial concentration, (c) PMS concentration, (c) pH, and (d) anions on PEC performance of NCD@CNFO. Conditions: [catalysts] = 285 mg cm⁻², $[Na_2SO_4]$ = 0.1 M, illumination density: 100 mW cm⁻², applied bias = 1.23 V vs. RHE.

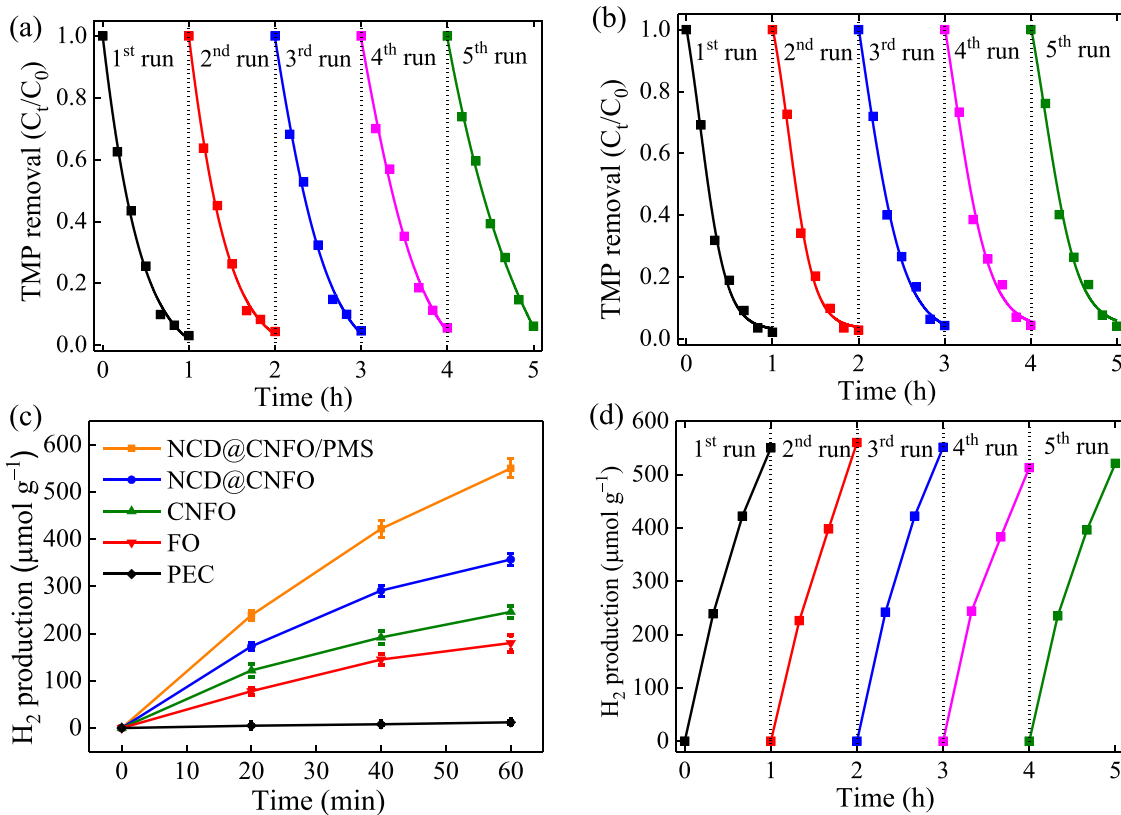
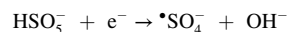
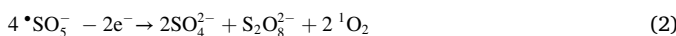


Fig. 8. PEC degradation of TMP on NCD@CNFO for five repeated runs (a) in aqueous solution, (b) in lake water, (c) H₂ production over different catalysts, and (d) PEC concurrent H₂ production over NCD@CNFO in TMP solution. Conditions: [catalysts] = 285 mg cm⁻², [TMP] = 0.05 mM, [PMS] = 0.1 mM, [Na₂SO₄] = 0.1 M, illumination density: 100 mW cm⁻², pH = 5 ± 0.1, applied bias = 1.23 V vs. RHE.

applied in actual environmental media.

3.4. PEC hydrogen evolution from water splitting

The PEC production of H₂ over different NCD@CNFO based nanocomposites was also investigated during the photocatalytic degradation of TMP in 0.1 M Na₂SO₄ solution with and without the activation of PMS. As presented in Fig. 8c, a very low yield of H₂ was obtained from water splitting in PEC system in the absence of the catalyst, which was consistent with TMP degradation efficiency. In the absence of PMS, the H₂ evolution rates were 180, 236, and 317 μmol cm⁻² h⁻¹ over FO, CNFO, and NCD@CNFO catalysts respectively. In contrast, the H₂ production rate by NCD@CNFO increased steadily with prolonged reaction time and reached 550 μmol cm⁻² h⁻¹ under PMS activation conditions. The enhancement of H₂ production rate in the presence of PMS is attributable to two reasons. First, chloride is a promoter for PMS activation, especially in acidic conditions. As mentioned in the experimental section, the pH of the solution during PEC experiments was kept at 5 by adding HCl. Therefore, the presence of Cl⁻ probably reacted with HSO₅⁻ to produce HOCl, which gave rise to the hydrogen evolution [54]. Second, the initiation of PMS activation might consume a h_{VB}⁺ on the catalyst surface to obtain ¹O₂ through reaction Eqs. (1) and (2) [55,56]. This means that the presence of PMS in the solution could reduce the e⁻-h⁺ recombination as well as donate an electron to the catalyst surface, increasing the current in the cathode (Pt counter electrode), which promoted the hydrogen production. Moreover, PMS might obtain an electron to transform into [•]SO₄⁻ as described in Eq. (3) to enhance TMP degradation.



Consequently, the superior activity of NCD@CNFO was fully demonstrated in the PEC system with respect to H₂ evolution and simultaneous organic degradation because of the efficient migration of charge carriers. Hence, the heterojunction system significantly improved the charge separation efficiency and provided the driving force for H₂ production from water splitting. This result is likely owing to the existence of NCD by its upconversion ability that could absorb a wide range of light and transferred electrons to combine with holes, leading to the reduction of electron-hole recombination. The stability of NCD@CNFO catalyst was demonstrated with 5 cycles. As shown in Fig. 8d, the H₂ production rates kept a constant level without significant change after the first 3 runs (550 μmol cm⁻² h⁻¹) and then maintained almost unchanged after 5 cycles and 94% (520 μmol cm⁻² h⁻¹) of initial performance. This result indicates that the NCD@CNFO is well stable and reusable to sustain PEC hydrogen production.

The composition of NCD@CNFO composite on the anode after 5 cycles of stability test for PEC degradation of TMP was examined. Fig. S6 reveals that the high-resolution XPS spectra of C 1 s, N 1 s, Fe 2p, and O 1 s of the NCD@CNFO after reaction were almost identical to those of the pristine sample, which means no change in the composition of the catalyst. In addition, the XRD pattern of NCD@CNFO catalyst after stability test (Fig. S7) also matched well with the initial one, confirming the intact structure of the catalyst. Although the catalyst exhibited good performance, further improvement should be needed and focused in our future work to meet the prerequisites for real-life applications.

3.5. Degradation pathway

HPLC-MS was used to identify the intermediates generated from the

degradation process of TMP over NCD@CNFO nanocomposite. The HPLC-MS chromatogram of the products is presented in Fig. S8 (Supplementary data), while the proposed degradation pathways of TMP over NCD@CNFO are presented in Fig. S9 (Supplementary data). The hydroxylation, demethylation, and cleavage were the primary reactions of the PEC degradation of TMP. Under hydroxylation, TMP could be readily attacked by $^1\text{O}_2$ and $\cdot\text{OH}$ radicals to produce 5-((2,4-diaminopyrimidin-5-yl)methyl)benzene-1,2,3,4-tetraol (*m/z* of 265), (2,4-diamino-1,2-dihydropyrimidin-5-yl)(3,4,5-trimethoxyphenyl)methanol (*m/z* of 309), and 2,6-diamino-5-(hydroxy(2-hydroxy-3,4,5-trimethoxyphenyl)methyl)-4,5-dihydropyrimidin-4-ol (*m/z* of 325) [57,58]. These products were further degraded to 5-vinylpyrimidine-2,4-diamine (*m/z* of 136), 2,4-diamino-5-(hydroxymethyl)-6-methylpyrimidin-1(2 H)-ol (*m/z* of 171), and 2,6-diamino-4,5-dihydropyrimidine-4,5-diol (*m/z* of 144) under the action of cleavage reaction with attack of $\cdot\text{O}_2$ [59]. Subsequently, 2,4-diamino-5-(3,4,5-trimethoxybenzyl)pyrimidin-1(2 H)-ol (*m/z* 309) was further oxidized and the pyrimidine ring was cut by $\cdot\text{OH}$ attack to form 2,4-diamino-5-((3,4,5-trimethoxy-cyclohexa-2,4-dien-1-yl)methyl)-5,6-dihydropyrimidine-1,6(2 H)-diol (*m/z* of 330) [11]. Additionally, some products including 2-amino-4-(hydroxyamino)-5-(hydroxymethyl)tetrahydropyrimidine-1,6(2 H)-diol (*m/z* of 195) and 2,6-diamino-5-(hydroxy(2-hydroxy-3,4,5-trimethoxyphenyl)methyl)-4,5-dihydropyrimidin-4-ol (*m/z* of 342) were generated after the hydroxylation/demethylation reactions by the attack of $\cdot\text{SO}_4^-$ to *m/z* 330 and *m/z* 309, respectively [60]. The final products of the degradation process were small molecules produced from oxidation or decomposition of C=C double bonds [61].

3.6. Possible mechanisms

3.6.1. Role of different reactive species

Scavenging experiments were employed to determine the predominant reactive species involved during the PEC degradation of TMP. Fig. 8a shows that the photoelectrochemical degradation was significantly inhibited by 1,4-benzoquinone (1,4-BQ) as the photodegradation

efficiency of TMP was only 46 %, depicting that $\cdot\text{O}_2^-$ radicals were the main species in this process. With the addition of tert-butanol (t-BuOH), the removal efficiency of TMP decreased to 55 %, indicating that $\cdot\text{OH}$ radicals were the second major reactive oxygen species. In the presence of ascorbic acid (AA), the oxidation efficiency of TMP was 60 %, which means the moderate contribution of $^1\text{O}_2$ to the degradation process. With the addition of KI and $\text{K}_2\text{Cr}_2\text{O}_7$, the photoelectrochemical performance remained at around 87 %, showing that h^+ and e^- contributed insignificantly to the TMP degradation. The contribution of holes generated in the valence band of FO to the degradation of TMP was negligible due to the restriction of the large number of electrons on the surface of NCD. To sum up, the sequence of the dominant reactive species participating in the degradation process was $\cdot\text{O}_2^- > \cdot\text{OH} > ^1\text{O}_2$.

3.6.2. EPR spin-trapping measurement

EPR was measured in methanol and aqueous solutions in the presence of 5,5-dimethyl-1-pyrroline-N-oxide (DMPO) to detect the presence of $\cdot\text{O}_2^-$ and $\cdot\text{OH}$, respectively. Fig. 9b-d show the EPR spectra of photodegradation of TMP over NCD@CNFO in the presence and absence of PMS. It is clear that no signal was found for all samples under the dark condition. After irradiation with UV light, the NCD@CNFO without the addition of PMS exhibited the characteristic 6-line spectrum in methanol, verifying the presence of DMPO- $\cdot\text{O}_2^-$ (Fig. 9b). It is interesting to note that the peak intensity of DMPO- $\cdot\text{O}_2^-$ adducts increased dramatically committed with the production of $\cdot\text{SO}_4^-$ peaks when PMS was added to the methanol. Besides, four characteristic peaks with the ratios of 1:2:2:1 were found in the solution, confirming the generation of $\cdot\text{OH}$ radicals (Fig. 8c). When 2,2,6,6-tetramethyl-1-piperidinyloxy (TEMPO) was used as the trapping agent of $^1\text{O}_2$, typical TEMPO- $^1\text{O}_2$ adducts peaks were observed in both NCD@CNFO spectra in the presence and absence of PMS (Fig. 8d) [62]. The intensities of DMPO- $\cdot\text{O}_2^-$, DMPO- $\cdot\text{OH}$, and TEMPO- $^1\text{O}_2$ adducts in PMS-mediated system were stronger than the pure NCD@CNFO, which was attributed to the generation of $\cdot\text{SO}_4^-$ radicals. Moreover, the singlet oxygen ($^1\text{O}_2$) could be produced by the self-decomposition of PMS (Eq. 4) [63] or from the

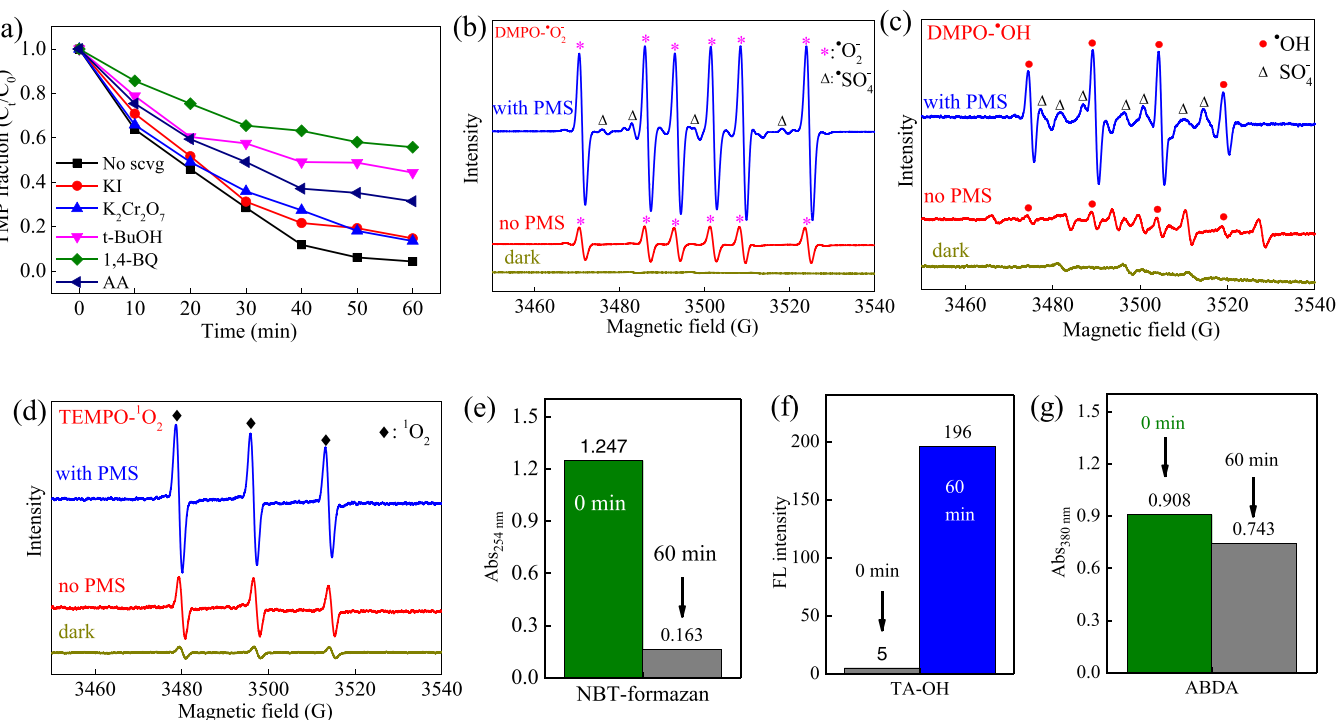
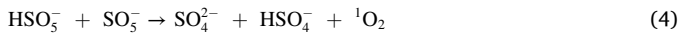


Fig. 9. (a) photoelectrochemical TMP degradation efficiency by NCD@CNFO in the presence of different scavengers, and EPR spin-trapping measurements of (b) DMPO- $\cdot\text{O}_2^-$, (c) DMPO- $\cdot\text{OH}$, and (d) TEMPO- $^1\text{O}_2$; (e), (f), (g) Reactive oxygen species quantification for NCD@CNFO: (e), NBT for $\cdot\text{O}_2^-$, (f) TA for $\cdot\text{OH}$, and (g) ABDA for $^1\text{O}_2$.

reaction of superoxide anion radicals ($\bullet\text{O}_2^-$) during the photocatalytic process (Eqs. 5 & 6) [64]:



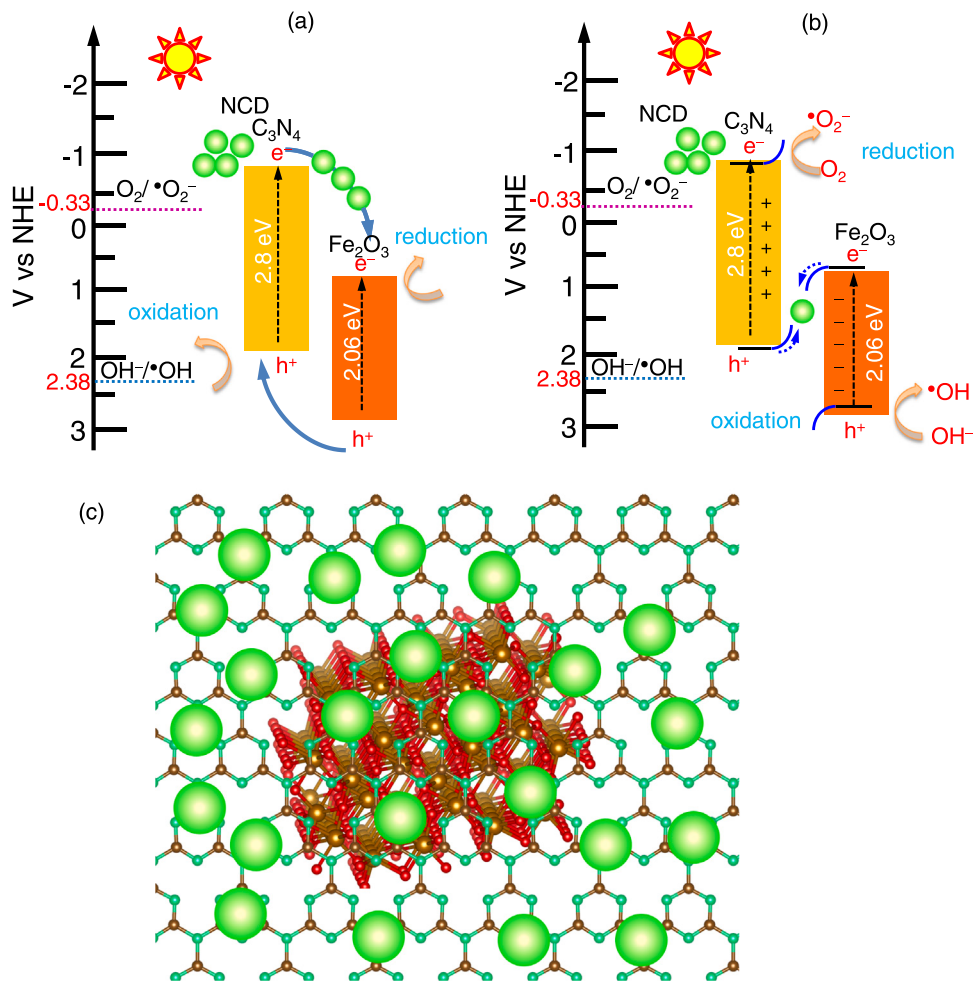
3.6.3. Quantity of reactive oxygen species (ROS)

The detailed experiment of the quantification of ROS was described in [Supplementary data](#). Briefly, Nitro blue tetrazolium chloride (NBT) was used to test $\bullet\text{O}_2^-$ radicals. Terephthalic acid (TA) was used as a probe to quantify $\bullet\text{OH}$ radicals. 9,10-anthracenediyl-bis(methylene)dimalonic acid (ABDA) was used to test $\bullet\text{O}_2$. As shown in [Fig. 9e](#), the reduction rate of absorbance of NBT/ $\bullet\text{O}_2^-$ was 86.9 %. By using the calibration curve in [Fig. 10a](#), the amount of $\bullet\text{O}_2^-$ was calculated as 1.13 μM . In [Fig. 9f](#), the amount of $\bullet\text{OH}$ radicals was quantified as 1.05 μM by measuring the increase in the FL intensity of TA and using the calibration curve ([Fig. S10b](#)). The quantity of singlet oxygen generated in the PEC system was determined using quantum yield calculation after 60 min reaction with ABDA under PEC/PMS condition [65]. As shown in [Fig. 9g](#), the reduction rate of absorbance of NCD@CNFO could be calculated as 18.2 %, then compared with that of methylene blue (MB), which has a 50 % quantum yield (QY) of singlet oxygen ([Fig. S10c](#)). Hence, the quantum yield of singlet oxygen generated by NCD@CNFO system, which could be calculated using [Eq. S5](#), was 12.2 %. These results agreed well with

the scavenging experiments and the proposed reaction equations, presenting that the generation of singlet oxygen from PMS and $\bullet\text{O}_2^-$ reaction.

3.6.4. Bandgap calculation

Mott-Schottky experiment was carried out to estimate the position of the conduction band of catalysts under the dark condition at a frequency of 1 kHz in 0.1 M Na_2SO_4 solution. [Fig. S10 \(Supplementary data\)](#) shows that all the photoelectrodes exhibited a positive slope, confirming that the as-prepared photocatalysts were n-type semiconductors. Moreover, the charge carrier density, derived from the slope of the tangent line of Mott-Schottky curves, gave the values of 1.56×10^9 , 2.98×10^{10} , 3.89×10^{10} for FO, CNFO, and NCD@CNFO, respectively, indicating that the addition of CN and NCD increased the charge carrier density of FO to enhance the charge transfer and separation efficiency. The intercept generated from an extended tangent line of Mott-Schottky curve with X-axis represented the flat band energy (E_{fb}) of the semiconductors, which means that the E_{fb} of FO and CN are 0.72 and -0.88 eV vs. SCE. The obtained potential could be effectively converted into the normal hydrogen electrode (NHE) using the Nernst equation: $E_{\text{NHE}} = E_{\text{SCE}} + 0.24$. Hence, the E_{fb} of FO and CN are 0.96 and -0.64 eV vs. NHE, respectively. Since the E_{CB} is more negative about -0.1 eV to -0.2 eV compared to the E_{fb} for n-type semiconductor, the E_{CB} of FO and CN were determined to be 0.76 and -0.84 eV, respectively. When combining the above result with the bandgap of FO and CN, the E_{VB} of FO and CN were calculated as 2.82 and 1.96 eV vs NHE, respectively ([Table S3, Supplementary data](#)).



Scheme 2. The proposed photocatalytic mechanisms for the NCD@CNFO: (a) type-II heterojunction, and (b) S-scheme; (c) structural configuration of NCD@CNFO composite.

The bandgap calculation results show that NCD@CNFO has a narrow bandgap, which can enable the harvest of long wavelength visible light to generate electron-hole pairs. Moreover, NCD is an excellent charge carrier that can decrease the $h^+ - e^-$ recombination to enhance photocatalytic efficiency. Considering the band structure of FO and CN, two possible separation processes including type-II or S-scheme heterojunctions were proposed. For type-II heterojunction (Scheme 2a), the photoexcited electrons in the CB of CN shell migrate to the CB of the FO core, while the photogenerated holes from the VB of the FO core would transfer to the VB of the CN shell. As a result, the electrons and holes were spatially separated. In this case, however, the electrons and holes had insufficient ability to produce ROS after charge transfer because the redox potentials of E_{VB} of CN (1.96 V) is lower than the potential to produce $\cdot OH$ ($E_{OH^-/\cdot OH} = 2.38$ V vs NHE) and the E_{CB} of FO (0.76 V) is more positive than that of superoxide anion radicals ($\cdot O_2^-$) ($E_{O_2/\cdot O_2^-} = -0.33$ V vs NHE). Therefore, the type-II heterojunction contradicts the experimental results as both $\cdot O_2^-$ and $\cdot OH$ cannot be produced in this scenario.

Scheme 2b illustrates the possible S-scheme for PEC system over NCD@CNFO nanocomposite. Owing to its upconversion property, NCD could absorb longer wavelengths (600–800 nm) from the irradiation source and emitted shorter wavelengths (300–450 nm) to improve the absorption efficiency of the as-prepared NCD@CNFO nanocomposite. The photoexcited electron-hole pairs were generated in both Fe_2O_3 and C_3N_4 under light excitation. The close contact from the shell/core structure induced electrons in $g-C_3N_4$ to migrate to Fe_2O_3 via interfaces. Thus, an internal electric field would be formed at the interfaces between $g-C_3N_4$ (positively charged) and Fe_2O_3 (negatively charged). In other words, electron donation appeared on $g-C_3N_4$ band edge, while electron acceptance appeared on Fe_2O_3 band edge. Subsequently, the Fermi level difference led to the band edges of $g-C_3N_4$ bend upward, while band edges of Fe_2O_3 bend downward. Under the excitation from photoelectrochemical energy, the electrons in the conduction band of Fe_2O_3 combined with the holes in the highest occupied molecular orbital (HOMO) of NCD, while the electrons in the lowest unoccupied molecular orbital (LUMO) of NCD migrated to the valence band of C_3N_4 . Thus, NCD served as the electron mediator and photosensitizer simultaneously [66, 67]. Accordingly, the electrons in conduction band of Fe_2O_3 could transfer to the interface and combine with the holes in the valence band of C_3N_4 within the internal electric field through the NCD mediator. As a result, an electron-rich region would be created in the CB of C_3N_4 . Because the potential energy of the CB of C_3N_4 ($E_{CB} = -0.84$ V) is more negative than $O_2/\cdot O_2^-$ (-0.33 V), $\cdot O_2^-$ radicals could be produced in the CB of C_3N_4 . Similarly, the enrichment of the photogenerated holes in the VB of Fe_2O_3 rendered the production of $\cdot OH$ radicals because the VB potential energy ($E_{VB} = 2.82$ V) is more positive than $\cdot OH/OH$ (2.34 V). Consequently, the NCD@CNFO shell/core nanocomposite could maintain oxidation of FO and reduction of C_3N_4 , which could further participate in the TMP degradation and H_2 production in solutions.

4. Conclusions

The NCD anchored CNFO shell/core nanocomposite has been successfully constructed by hydrothermal and physical self-assembly strategies. The NCD@CNFO nanocomposite has shown its superior capability in enhancing the photoelectrochemical degradation of TMP and hydrogen production simultaneously, both in an aqueous solution and in real water. The photocurrent density was 3.07 mA cm^{-2} at 1.6 V vs NHE, likely attributed to the fact that the narrow band gap of CNFO could absorb long wavelength, and the incorporation of NCD significantly promoted the PEC performance due to its up-conversion and electron transfer mediating properties. This process resulted in the generation of a large number of electron-hole pairs to effectively participate in the photoelectrocatalytic reactions for TMP degradation and H_2 evolution from water splitting. The mildly acidic solution at pH 5 was the optimal condition for activating PMS to produce radicals for the

photoelectrochemical activity. An S-scheme was proposed to clarify the catalytic mechanism for TMP degradation and H_2 production over NCD@CNFO composite. The results clearly signify the superiority of NCD@CNFO nanocomposite to PEC reaction, and can open avenues to design photocatalysts that can solve the two hottest issues, namely renewable energy scarcity and environmental pollution.

CRediT authorship contribution statement

Van Dien Dang: Conceptualization, Data curation, Formal analysis, Writing – original draft, Investigation, Methodology, Resources, Software, Validation, Visualization, Writing – review & editing. **Thamilselvan Annadurai:** Data curation, Methodology, Investigation. **Akhil Pradiprao Khedulkar:** Data curation, Methodology, Investigation. **Jui-Yen Lin:** Data curation, Methodology, Investigation. **Joemer Adorna Jr:** Data curation, Methodology, Investigation. **Wan-Ju Yu:** Data curation, Methodology, Investigation. **Bidhan Pandit:** Data curation, Investigation, Validation, Visualization, Writing – review & editing. **Trung Viet Huynh:** Data curation, Methodology, Investigation. **Ruey-an Doong:** Conceptualization, Investigation, Validation, Visualization, Writing – review & editing, Supervision.

Declaration of Competing Interest

The authors declare that they have no known competing financial interests or personal relationships that could have appeared to influence the work reported in this paper.

Data availability

Data will be made available on request.

Acknowledgements

The authors thank the National Science and Technology Council (NSTC), Taiwan, for financial support under grant No 111-2223-E-007-008. We also thank EPR analysis service from Instrumentation Center at National Tsinghua University (NTNU); and mass spectrometry analysis from Mass Laboratory, National Yang Ming Chiao Tung University (NYCU), Hsinchu, Taiwan.

Appendix A. Supporting information

Supplementary data associated with this article can be found in the online version at [doi:10.1016/j.apcatb.2022.121928](https://doi.org/10.1016/j.apcatb.2022.121928).

References

- [1] V.M. Vaughn, T.N. Gandhi, V. Chopra, L.A. Petty, D.L. Giesler, A.N. Malani, S. J. Bernstein, L.M. Hsaiky, J.M. Pogue, L. Dumkow, Antibiotic overuse after hospital discharge: a multi-hospital cohort study, *Clin. Infect. Dis.* 73 (2020) 4499–4506.
- [2] M. Wang, Z. Wang, X. Gong, Z. Guo, The intensification technologies to water electrolysis for hydrogen production – a review, *Renew. Sustain. Energy Rev.* 29 (2014) 573–588.
- [3] S.D. Tilley, Recent advances and emerging trends in photo-electrochemical solar energy conversion, *Adv. Energy Mater.* 9 (2019), 1802877.
- [4] J. Liu, J. Li, Y. Li, J. Guo, S.-M. Xu, R. Zhang, M. Shao, Photoelectrochemical water splitting coupled with degradation of organic pollutants enhanced by surface and interface engineering of $BiVO_4$ photoanode, *Appl. Catal. B Environ.* 278 (2020), 119268.
- [5] S.K. Saraswat, D.D. Rodene, R.B. Gupta, Recent advancements in semiconductor materials for photoelectrochemical water splitting for hydrogen production using visible light, *Renew. Sustain. Energy Rev.* 89 (2018) 228–248.
- [6] J. Fu, J. Yu, C. Jiang, B. Cheng, $g-C_3N_4$ -based heterostructured photocatalysts, *Adv. Energy Mater.* 8 (2018), 1701503.
- [7] M. Zhang, X. Bai, D. Liu, J. Wang, Y. Zhu, Enhanced catalytic activity of potassium-doped graphitic carbon nitride induced by lower valence position, *Appl. Catal. B Environ.* 164 (2015) 77–81.
- [8] X. Chen, J. Zhang, X. Fu, M. Antonietti, X. Wang, Fe- $g-C_3N_4$ -catalyzed oxidation of benzene to phenol using hydrogen peroxide and visible light, *J. Am. Chem. Soc.* 131 (2009) 11658–11659.

[9] J. Li, S.K. Cushing, J. Bright, F. Meng, T.R. Senty, P. Zheng, A.D. Bristow, N. Wu, $\text{Ag}/\text{Cu}_2\text{O}$ core-shell nanoparticles as visible-light plasmonic photocatalysts, *ACS Catal.* 3 (2013) 47–51.

[10] K. Mondal, A. Sharma, Recent advances in the synthesis and application of photocatalytic metal–metal oxide core–shell nanoparticles for environmental remediation and their recycling process, *RSC Adv.* 6 (2016) 83589–83612.

[11] R. Li, J. Huang, M. Cai, J. Huang, Z. Xie, Q. Zhang, Y. Liu, H. Liu, W. Lv, G. Liu, Activation of peroxymonosulfate by Fe doped $\text{g-C}_3\text{N}_4$ /graphene under visible light irradiation for Trimethoprim degradation, *J. Hazard. Mater.* 384 (2020), 121435.

[12] X. She, J. Wu, H. Xu, J. Zhong, Y. Wang, Y. Song, K. Nie, Y. Liu, Y. Yang, M.T. F. Rodrigues, High efficiency photocatalytic water splitting using 2D $\alpha\text{-Fe}_2\text{O}_3/\text{g-C}_3\text{N}_4$ Z-scheme catalysts, *Adv. Energy Mater.* 7 (2017), 170025.

[13] T. Guo, K. Wang, G. Zhang, X. Wu, A novel $\alpha\text{-Fe}_2\text{O}_3@/\text{g-C}_3\text{N}_4$ catalyst: synthesis derived from Fe-based MOF and its superior photo-Fenton performance, *Appl. Surf. Sci.* 469 (2019) 331–339.

[14] Y. Geng, D. Chen, N. Li, Q. Xu, H. Li, J. He, J. Lu, Z-Scheme 2D/2D $\alpha\text{-Fe}_2\text{O}_3/\text{g-C}_3\text{N}_4$ heterojunction for photocatalytic oxidation of nitric oxide, *Appl. Catal. B* 280 (2021), 119409.

[15] Y. Li, S. Zhu, Y. Liang, Z. Li, S. Wu, C. Chang, S. Luo, Z. Cui, Synthesis of $\alpha\text{-Fe}_2\text{O}_3/\text{g-C}_3\text{N}_4$ photocatalyst for high-efficiency water splitting under full light, *Mater. Des.* 196 (2020), 109191.

[16] A.E.A. Bakr, W.M. El Rouby, M.D. Khan, A.A. Farghali, B. Xulu, N. Revaprasadu, Synthesis and characterization of Z-scheme $\alpha\text{-Fe}_2\text{O}_3$ NTs/ruptured tubular $\text{g-C}_3\text{N}_4$ for enhanced photoelectrochemical water oxidation, *J. Sol. Energy* 193 (2019) 403–412.

[17] Q. Xu, B. Zhu, C. Jiang, B. Cheng, J. Yu, Constructing 2D/2D $\text{Fe}_2\text{O}_3/\text{g-C}_3\text{N}_4$ direct Z-scheme photocatalysts with enhanced H_2 generation performance, *Sol. RRL* 2 (2018), 1800006.

[18] J. Wang, X. Zuo, W. Cai, J. Sun, X. Ge, H. Zhao, Facile fabrication of direct solid-state Z-scheme $\text{g-C}_3\text{N}_4/\text{Fe}_2\text{O}_3$ heterojunction: a cost-effective photocatalyst with high efficiency for the degradation of aqueous organic pollutants, *Dalton Trans.* 47 (2018) 15382–15390.

[19] A. Iwase, Y.H. Ng, Y. Ishiguro, A. Kudo, R. Amal, Reduced graphene oxide as a solid-state electron mediator in Z-scheme photocatalytic water splitting under visible light, *J. Am. Chem. Soc.* 133 (2011) 11054–11057.

[20] Y. Liu, Q. Zhu, M. Tayyab, L. Zhou, J. Lei, J. Zhang, Single-atom Pt loaded Zinc vacancies ZnO-ZnS induced type-V electron transport for efficiency photocatalytic H_2 , *Evol. Sol. RRL* 5 (2021), 2100536.

[21] K. Akbar, E. Moretti, A. Vomiero, Carbon dots for photocatalytic degradation of aqueous pollutants: recent advancements, *Adv. Opt. Mater.* 9 (2021), 2100532.

[22] Q. Dang, Y. Sun, X. Wang, W. Zhu, Y. Chen, F. Liao, H. Huang, M. Shao, Carbon dots-Pt modified polyaniline nanosheet grown on carbon cloth as stable and high-efficient electrocatalyst for hydrogen evolution in pH-universal electrolyte, *Appl. Catal. B Environ.* 257 (2019), 117905.

[23] K. Hola, M. Sudolska, S. Kalytchuk, D. Nachtigallova, A.L. Rogach, M. Otyepka, R. Zboril, Graphitic nitrogen triggers red fluorescence in carbon dots, *ACS Nano* 11 (2017) 12402–12410.

[24] P. Chen, F. Wang, Z.-F. Chen, Q. Zhang, Y. Su, L. Shen, K. Yao, Y. Liu, Z. Cai, W. Lv, G. Liu, Study on the photocatalytic mechanism and detoxicity of gemfibrozil by a sunlight-driven TiO_2 /carbon dots photocatalyst: the significant roles of reactive oxygen species, *Appl. Catal. B Environ.* 204 (2017) 250–259.

[25] R. Shi, Z. Li, H. Yu, L. Shang, C. Zhou, G.I. Waterhouse, L.Z. Wu, T. Zhang, Effect of nitrogen doping level on the performance of N-doped carbon quantum dot/ TiO_2 composites for photocatalytic hydrogen evolution, *ChemSusChem* 10 (2017) 4650–4656.

[26] X. Huang, L. Yang, S. Hao, B. Zheng, L. Yan, F. Qu, A.M. Asiri, X. Sun, N-doped carbon dots: a metal-free co-catalyst on hematite nanorod arrays toward efficient photoelectrochemical water oxidation, *Inorg. Chem. Front.* 4 (2017) 537–540.

[27] H. Han, F. Karlicky, S. Pitchaimuthu, S.H.R. Shin, A. Chen, Highly ordered N-doped carbon dots photosensitizer on metal–organic framework-decorated ZnO nanotubes for improved photoelectrochemical water splitting, *Small* 15 (2019), 1902771.

[28] Y. Sun, Z. Zhang, A. Xie, C. Xiao, S. Li, F. Huang, Y. Shen, An ordered and porous N-doped carbon dot-sensitized Bi_2O_3 inverse opal with enhanced photoelectrochemical performance and photocatalytic activity, *Nanoscale* 7 (2015) 13974–13980.

[29] W. Kong, X. Zhang, S. Liu, Y. Zhou, B. Chang, S. Zhang, H. Fan, B. Yang, N doped carbon dot modified WO_3 nanoflakes for efficient photoelectrochemical water oxidation, *Adv. Mater. Interfaces* 6 (2019), 1801653.

[30] V.D. Dang, A.B. Gangaboina, R.-A. Doong, Bipyridine-and copper-functionalized N-doped carbon dots for fluorescence turn off-on detection of ciprofloxacin, *ACS Appl. Mater. Interfaces* 12 (2020) 32247–32258.

[31] Y. Liu, L. Jiang, B. Li, X. Fan, W. Wang, P. Liu, S. Xu, X. Luo, Nitrogen doped carbon dots: mechanism investigation and their application for label free CA125 analysis, *J. Mater. Chem. B* 7 (2019) 3053–3058.

[32] C. Xia, M. Cao, J. Xia, G. Zhou, D. Jiang, D. Zhang, J. Wang, H. Li, An ultrafast responsive and sensitive ratiometric fluorescent pH nanoprobe based on label-free dual-emission carbon dots, *J. Mater. Chem. C* 7 (2019) 2563–2569.

[33] Y. Qiu, S.-F. Leung, Q. Zhang, B. Hua, Q. Lin, Z. Wei, K.-H. Tsui, Y. Zhang, S. Yang, Z. Fan, Efficient photoelectrochemical water splitting with ultrathin films of hematite on three-dimensional nanophotonic structures, *Nano Lett.* 14 (2014) 2123–2129.

[34] R. Parvari, F. Ghorbani-Shahna, A. Bahrami, S. Azizian, M.J. Assari, M. Farhadian, A novel core-shell structured $\alpha\text{-Fe}_2\text{O}_3/\text{Cu}/\text{g-C}_3\text{N}_4$ nanocomposite for continuous photocatalytic removal of air ethylbenzene under visible light irradiation, *J. Photochem. Photobiol. A* 399 (2020), 112643.

[35] V.D. Dang, J. Adorna Jr, T. Annadurai, T.A.N. Bui, H.L. Tran, L.-Y. Lin, R.-A. Doong, Indirect Z-scheme nitrogen-doped carbon dot decorated $\text{Bi}_2\text{MoO}_6/\text{g-C}_3\text{N}_4$ photocatalyst for enhanced visible-light-driven degradation of ciprofloxacin, *Chem. Eng. J.* 422 (2021), 130103.

[36] S. Xiong, X. Liu, X. Zhu, G. Liang, Z. Jiang, B. Cui, J. Bai, One-step preparation of well-dispersed spindle-like Fe_2O_3 nanoparticles on $\text{g-C}_3\text{N}_4$ as highly efficient photocatalysts, *Ecotoxicol. Environ. Saf.* 208 (2020), 111519.

[37] M. Thommes, K. Kaneko, A.V. Neimark, J.P. Olivier, F. Rodriguez-Reinoso, J. Rouquerol, K.S. Sing, Physisorption of gases, with special reference to the evaluation of surface area and pore size distribution (IUPAC Technical Report), *Pure Appl. Chem.* 87 (2015) 1051–1069.

[38] L. Chen, X. Yang, J. Chen, J. Liu, H. Wu, H. Zhan, C. Liang, M. Wu, Continuous shape-and spectroscopy-tuning of hematite nanocrystals, *Inorg. Chem.* 49 (2010) 8411–8420.

[39] Y.-F. Guan, B.-C. Huang, C. Qian, H.-Q. Yu, Quantification of humic substances in natural water using nitrogen-doped carbon dots, *Environ. Sci. Technol.* 51 (2017) 14092–14099.

[40] G.F. Moreira, E.R. Peçanha, M.B. Monte, L.S. Leal Filho, F. Stavale, XPS study on the mechanism of starch-hematite surface chemical complexation, *Miner. Eng.* 110 (2017) 96–103.

[41] S.-S. Yi, J.-M. Yan, Q. Jiang, Carbon quantum dot sensitized integrated $\text{Fe}_2\text{O}_3@/\text{g-C}_3\text{N}_4$ core–shell nanoarray photoanode towards highly efficient water oxidation, *J. Mater. Chem. A* 6 (2018) 9839–9845.

[42] G. Liu, M. Feng, M. Tayyab, J. Gong, M. Zhang, M. Yang, K. Lin, Direct and efficient reduction of perfluorooctanoic acid using bimetallic catalyst supported on carbon, *J. Hazard. Mater.* 412 (2021), 125224.

[43] S. Chen, J. Duan, J. Ran, S.Z. Qiao, Paper-based N-doped carbon films for enhanced oxygen evolution electrocatalysis, *Adv. Sci.* 2 (2015), 1400015.

[44] L. Zhang, X. Zhang, C. Wei, F. Wang, H. Wang, Z. Bian, Interface engineering of Z-scheme $\alpha\text{-Fe}_2\text{O}_3/\text{g-C}_3\text{N}_4$ photoanode: simultaneous enhancement of charge separation and hole transportation for photoelectrocatalytic organic pollutant degradation, *Chem. Eng. J.* 435 (2022), 134873.

[45] M. Tayyab, Y. Liu, S. Min, R. Muhammad Irfan, Q. Zhu, L. Zhou, J. Lei, J. Zhang, Simultaneous hydrogen production with the selective oxidation of benzyl alcohol to benzaldehyde by a noble-metal-free photocatalyst VC/CdS nanowires, *Chin. J. Catal.* 43 (2022) 1165–1175.

[46] Y. Tang, J. Huang, M. Jiang, J. Yu, Q. Wang, J. Zhao, J. Li, X. Yu, J. Zhao, Photo-induced synthesis of nanostructured Pt-on-Au/ $\text{g-C}_3\text{N}_4$ composites for visible light photocatalytic hydrogen production, *J. Mater. Sci.* 55 (2020) 15574–15587.

[47] H. Shao, Y. Wang, H. Zeng, J. Zhang, Y. Wang, M. Sillanpää, X. Zhao, Enhanced photoelectrocatalytic degradation of bisphenol A by BiVO_4 photoanode coupling with peroxymonosulfate, *J. Hazard. Mater.* 394 (2020), 121105.

[48] C. Liu, S. Mao, H. Wang, Y. Wu, F. Wang, M. Xia, Q. Chen, Peroxymonosulfate-assisted for facilitating photocatalytic degradation performance of 2D/2D WO_3/BiOBr S-scheme heterojunction, *Chem. Eng. J.* 430 (2022), 132806.

[49] Y. Wang, X. Zhao, D. Cao, Y. Wang, Y. Zhu, Peroxymonosulfate enhanced visible light photocatalytic degradation bisphenol A by single-atom dispersed Ag mesoporous $\text{g-C}_3\text{N}_4$ hybrid, *Appl. Catal. B Environ.* 211 (2017) 79–88.

[50] G. Fan, R. Ning, Z. Yan, J. Luo, B. Du, J. Zhan, L. Liu, J. Zhang, Double photoelectron-transfer mechanism in $\text{Ag}-\text{AgCl}/\text{WO}_3/\text{g-C}_3\text{N}_4$ photocatalyst with enhanced visible-light photocatalytic activity for trimethoprim degradation, *J. Hazard. Mater.* 403 (2021), 123964.

[51] T.N. Das, Reactivity and role of SO_4^{2-} radical in aqueous medium chain oxidation of sulfite to sulfate and atmospheric sulfuric acid generation, *J. Phys. Chem. A* 105 (2001) 9142–9155.

[52] Z. Qiang, C. Adams, Potentiometric determination of acid dissociation constants (pKa) for human and veterinary antibiotics, *Water Res.* 38 (2004) 2874–2890.

[53] Y.-H. Guan, J. Ma, X.-C. Li, J.-Y. Fang, L.-W. Chen, Influence of pH on the formation of sulfate and hydroxyl radicals in the UV/peroxymonosulfate system, *Environ. Sci. Technol.* 45 (2011) 9308–9314.

[54] C. Gao, X. Feng, L. Yi, X. Wu, R. Zheng, G. Zhang, Y. Li, Peroxymonosulfate activation based on $\text{CoS}_8@-\text{N-C}$: a new strategy for highly efficient hydrogen production and synchronous formaldehyde removal in wastewater, *J. Mater. Sci. Technol.* 127 (2022) 256–267.

[55] M. Cui, K. Cui, X. Liu, X. Chen, Z. Guo, Y. Chen, C.-x. Li, Insights into the photocatalytic peroxymonosulfate activation over defective boron-doped carbon nitride for efficient pollutants degradation, *J. Hazard. Mater.* 418 (2021), 126338.

[56] Y. Gao, Y. Zhu, L. Lyu, Q. Zeng, X. Xing, C. Hu, Electronic structure modulation of graphitic carbon nitride by oxygen doping for enhanced catalytic degradation of organic pollutants through peroxymonosulfate activation, *Environ. Sci. Technol.* 52 (2018) 14371–14380.

[57] X. Luo, Z. Zheng, J. Greaves, W.J. Cooper, W. Song, Trimethoprim: kinetic and mechanistic considerations in photochemical environmental fate and AOP treatment, *Water Res.* 46 (2012) 1327–1336.

[58] F.C. Moreira, R.A.R. Boaventura, E. Brillas, V.J.P. Vilar, Degradation of trimethoprim antibiotic by UVA photoelectro-Fenton process mediated by $\text{Fe}(\text{III})$ -carboxylate complexes, *Appl. Catal. B Environ.* 162 (2015) 34–44.

[59] Y. Ji, W. Xie, Y. Fan, Y. Shi, D. Kong, J. Lu, Degradation of trimethoprim by thermo-activated persulfate oxidation: reaction kinetics and transformation mechanisms, *Chem. Eng. J.* 286 (2016) 16–24.

[60] G. Fan, R. Ning, Z. Yan, J. Luo, B. Du, J. Zhan, L. Liu, J. Zhang, Double photoelectron-transfer mechanism in $\text{Ag}-\text{AgCl}/\text{WO}_3/\text{g-C}_3\text{N}_4$ photocatalyst with enhanced visible-light photocatalytic activity for trimethoprim degradation, *J. Hazard. Mater.* 403 (2021), 123964.

- [61] L. Hu, A.M. Stemig, K.H. Wammer, T.J. Strathmann, Oxidation of antibiotics during water treatment with potassium permanganate: reaction pathways and deactivation, *Environ. Sci. Technol.* 45 (2011) 3635–3642.
- [62] Q. Liu, T. Chen, Y. Guo, Z. Zhang, X. Fang, Grafting Fe (III) species on carbon nanodots/Fe-doped g-C₃N₄ via interfacial charge transfer effect for highly improved photocatalytic performance, *Appl. Catal. B Environ.* 205 (2017) 173–181.
- [63] Y. Zhou, J. Jiang, Y. Gao, J. Ma, S.-Y. Pang, J. Li, X.-T. Lu, L.-P. Yuan, Activation of peroxymonosulfate by benzoquinone: a novel nonradical oxidation process, *Environ. Sci. Technol.* 49 (2015) 12941–12950.
- [64] J.M. Burns, W.J. Cooper, J.L. Ferry, D.W. King, B.P. DiMento, K. McNeill, C. J. Miller, W.L. Miller, B.M. Peake, S.A. Rusak, Methods for reactive oxygen species (ROS) detection in aqueous environments, *Aquat. Sci.* 74 (2012) 683–734.
- [65] L.-T. Yen, C.-H. Weng, N.A.T. Than, J.-H. Tzeng, A.R. Jacobson, K. Iamsaard, V. D. Dang, Y.-T. Lin, Mode of inactivation of *Staphylococcus aureus* and *Escherichia coli* by heated oyster-shell powder, *Chem. Eng. J.* 432 (2022), 134386.
- [66] J. Liu, Y. Liu, N. Liu, Y. Han, X. Zhang, H. Huang, Y. Lifshitz, S.-T. Lee, J. Zhong, Z. Kang, Metal-free efficient photocatalyst for stable visible water splitting via a two-electron pathway, *Science* 347 (2015) 970–974.
- [67] P. Zhang, T. Wang, X. Chang, L. Zhang, J. Gong, Synergistic cocatalytic effect of carbon nanodots and Co₃O₄ nanoclusters for the photoelectrochemical water oxidation on hematite, *Angew. Chem.* 128 (2016) 5945–5949.



Van Dien Dang received his Ph.D. degree in Environmental Engineering from National Yang Ming Chiao Tung University, Taiwan (2021) under the supervision of Prof. Ruey-an Doong. He is a tenured lecturer at Ho Chi Minh City University of Food Industry (HUF), Vietnam. His research focuses on synthesizing nanomaterials for multiple applications such as sensing, catalysis, water splitting, and supercapacitor.



Akhil Pradiprao Khedulkar completed his Master's degree in chemistry from Rashtrasant Tukadoji Maharaj Nagpur University, Nagpur, India in 2015. After his Master's, Akhil joined as a Project Assistant at CSIR-National Environmental Engineering Research Institute (CSIR-NEERI), Nagpur, India, where he was a part of various national and international projects in the field of solid and hazardous waste management. He is currently pursuing a Ph.D. in Biomedical Engineering and Environmental Science at National Tsing Hua University, Taiwan, under the supervision of Professor Ruey-An Doong. His current research focus on the fabrication of renewable and sustainable devices from high-valued agricultural waste biochar's for supercapacitor applications.



Bidhan Pandit is now a Marie Curie CONEX-Plus researcher at University Carlos III de Madrid (UC3M), Madrid, Spain. He received his Ph.D. degree (2019) in Physics from Visvesvaraya National Institute of Technology (India) and joined as CNRS Postdoctoral Research Fellow at the Institut Charles Gerhardt Montpellier (ICGM), Université de Montpellier (France). His previous scientific interests focus on the synthesis of nanostructures and fabrication of flexible devices for supercapacitor applications. His current research focus includes the synthesis of cathode materials for lithium, sodium and potassium-ion batteries, as well as the *in situ/operando* X-ray based characterizations for the understanding of battery mechanisms.



Ruey-An Doong is a chair professor in the Institute of Analytical and Environmental Sciences, National Tsing Hua University, Taiwan. He is also the Dean of Tsing Hua International College. His current research interest includes the fabrication of nanomaterials with novel optical and electrochemical properties for biosensing of analytes, environmentally benign nanotechnology for treatment of contaminants, and porous materials for energy storage and conversion. More recently, his research work also focused on the water-energy nexus and the fabrication of high-valued biochar's from agricultural waste for water and energy application.